The selection function of the Gaia DR3 open cluster census*

Emily L. Hunt^{1,2}, Tristan Cantat-Gaudin², Friedrich Anders^{3,4,5}, Sagar Malhotra^{3,4,5}, Lorenzo Spina^{6,7}, Alfred Castro-Ginard^{3,4,5}, and Lorenzo Cavallo⁸

- ¹ Department of Astrophysics, University of Vienna, Türkenschanzstrasse 17, 1180 Wien, Austria e-mail: emily.lauren.hunt@univie.ac.at
- ² Max-Planck-Institut für Astronomie, Königstuhl 17, 69117 Heidelberg, Germany
- Departament de Física Quàntica i Astrofísica (FQA), Universitat de Barcelona (UB), Martí i Franquès, 1, 08028 Barcelona, Spain
- ⁴ Institut de Ciències del Cosmos (ICCUB), Universitat de Barcelona (UB), Martí i Franquès, 1, 08028 Barcelona, Spain
- ⁵ Institut d'Estudis Espacials de Catalunya (IEEC), Edifici RDIT, Campus UPC, 08860 Castelldefels (Barcelona), Spain
- ⁵ INAF, Osservatorio Astrofisico di Arcetri, Largo E. Fermi 5, 50125 Firenze, Italy
- INAF, Osservatorio Astronomico di Padova, Vicolo dell'Osservatorio 5, 35122 Padova, Italy
- Dipartimento di Fisica e Astronomia, Università di Padova, Vicolo dell'Osservatorio 3, 35122 Padova, Italy

Received 21 October 2025; accepted ??

ABSTRACT

Context. Open clusters are among the most useful and widespread tracers of Galactic structure. The completeness of the Galactic open cluster census, however, remains poorly understood.

Aims. For the first time ever, we establish the selection function of an entire open cluster census, publishing our results as an open-source Python package for use by the community. Our work is valid for the Hunt & Reffert catalogue of clusters in Gaia DR3. Methods. We developed and open-sourced our cluster simulator from our first work. Then, we performed 80 590 injection and retrievals of simulated open clusters to test the Hunt & Reffert catalogue's sensitivity. We fit a logistic model of cluster detectability that depends only on a cluster's number of stars, median parallax error, Gaia data density, and a user-specified significance threshold. Results. We find that our simple model accurately predicts cluster detectability, with a 94.53% accuracy on our training data that is comparable to a machine-learning based model with orders of magnitude more parameters. Our model itself offers numerous insights on why certain clusters are detected. We briefly use our model to show that cluster detectability depends on non-intuitive parameters, such as a cluster's proper motion, and we show that even a modest 25 km/s boost to a cluster's orbital speed can result in an almost 3× higher detection probability, depending on its position. In addition, we publish our raw cluster injection and retrievals and cluster memberships, which could be used for a number of other science cases – such as estimating cluster membership incompleteness. Conclusions. Using our results, selection effect-corrected studies are now possible with the open cluster census. Our work will enable a number of brand new types of study, such as detailed comparisons between the Milky Way's cluster census and recent extragalactic cluster samples.

Key words. open clusters and associations: general – Methods: data analysis – Galaxy: disk – Galaxy: evolution

1. Introduction

As the only galaxy that we observe from within, the Milky Way is a uniquely challenging galaxy to study. Nevertheless, our unique place in the Milky Way also allows for significantly more detailed observations of its content. To accurately untangle our Galaxy's structure from the solar system, tracers with accurate distance information are essential. Open clusters (OCs) are among the most prolific such tracers. As single populations of stars with ages usually no higher than 1 Gyr (Wielen 1971; Pandey & Mahra 1986; Lamers & Gieles 2006; Anders et al. 2021), the parameters of OCs can be inferred to much greater precision than for individual field stars – either by averaging over all N stars in a cluster to derive a measurement around \sqrt{N} times more accurate, or by using a cluster's colour-magnitude diagram (CMD) to fit isochrones and derive a precise age or extinction value (Demarque & Larson 1964; Kharchenko et al. 2013; Cantat-Gaudin & Casamiquela 2024).

In the era of *Gaia* (Gaia Collaboration et al. 2016), the potential of OCs as Galactic tracers has only increased. The billionstar astrometric and photometric data from Gaia's second and third data releases (Gaia Collaboration et al. 2018, 2023) has enabled the discovery of thousands of new OCs since the release of Gaia DR2 (e.g. Castro-Ginard et al. 2018, 2019, 2020, 2022; Sim et al. 2019; Liu & Pang 2019; Hunt & Reffert 2021, 2023). At the same time, the cluster census itself has improved in quality, with over a thousand OCs from before Gaia having been ruled out as asterisms (Cantat-Gaudin & Anders 2020; Hunt & Reffert 2023, hereafter HR23). Despite these large improvements in the size of the OC census, modern OC catalogues are still highly incomplete. Extrapolating from the roughly complete solar neighbourhood, the Milky Way probably contains around 10° OCs (Dias et al. 2002; Bonatto et al. 2006; Kharchenko et al. 2013; Hunt & Reffert 2024), and the latest OC catalogues contain barely 5% of this total number of clusters (e.g. Hunt & Reffert 2024, hereafter HR24), as extinction, crowding, and distance present firm limits on OC detectability.

Studies that wish to infer some property of the Milky Way based on its observed population of OCs must hence reckon with

^{*} Our models are available as a Python package at https://github.com/emilyhunt/hr_selection_function.

working with a largely incomplete cluster sample. Traditionally, the completeness issue was avoided by considering a volume-limited complete sample of clusters, usually by looking at the volume distribution of clusters and setting the completeness-limited radius to the point at which this distribution begins to fall. However, this self-driven method is inherently limited for two reasons: firstly, it is 'data-wasteful,' as the majority of a catalogue (outside of the 100% completeness radius) must be discarded; and secondly, as it is insensitive to unknown incompletenesses or structure in a given dataset, this method is likely to produce incorrect results (Rix et al. 2021). A more statistically rigorous approach is to derive the selection function of a given catalogue, which estimates the probability that a cluster with parameters θ will be detected by a given survey, $P(\text{detected} \mid \theta)$.

Before the advent of *Gaia*, cluster catalogues compiled results from many different inhomogeneous surveys into a single work – meaning that they would have a complicated selection function composed of each individual included survey. Modern machine learning techniques and clustering algorithms, which are now commonplace for recovering OCs (e.g. Castro-Ginard et al. 2018; Hunt & Reffert 2023), present an advantage: a single technique can detect a majority of the cluster population and create a single, homogeneous catalogue, which in turn will have a single selection function that could be determined.

In this work, we build upon our previous prototype work in the Galactic anticentre (Hunt et al. 2025, hereafter Paper I) and construct a selection function for the entire HR24 cluster catalogue, using an injection and retrieval-based method. To do so, we simulate injection and retrieval following the clustering method of HR23, which the HR24 catalogue is constructed from. We show how seemingly innocuous facets of the OC census (such as its velocity distribution) can be severely impacted by not considering incompleteness. We publish an open-source Python implementation of our model for use by the community. We outline our approach and our cluster simulator in Sect. 2, deriving a selection function that depends on the number of stars in a cluster in Sect. 3. We provide a fast additional way to simulate the number of stars a cluster would have based on its parameters in Sect. 4. We show an example application of our selection function to show the impact of velocity on cluster detectability in Sect. 5. Section 6 discusses important caveats, best practices, and areas for future improvement of our model, concluded in Sect. 7. For particularly keen readers, the Appendices of this work include extended information, such as: a number of example Python snippets for querying our model or simulating clusters, and advice for future cluster selection functions and cluster catalogues to make selection functions easier to determine.

2. Cluster injection and retrieval strategy

In this section, we outline how we simulated, injected, and retrieved OCs to replicate the HR23 cluster recovery pipeline and derive its selection function. We begin with a brief recap of our Paper I cluster simulation technique, before discussing additional features added to it to improve the legacy value of our published data of simulated and retrieved clusters. We then outline the parameter ranges explored in this work.

2.1. Recap of Paper I cluster simulation pipeline

In Paper I, we created a cluster simulation pipeline to simulate OCs across a wide range of parameters. We simulate OCs based on the assumptions and models recapped here; we refer

the reader to Paper I for a thorough explanation. To derive absolute cluster photometry for a given cluster, we begin by interpolating PARSEC v1.2s isochrones (Bressan et al. 2012) to a given cluster age $\log_{10} t$ and metallicity [M/H], then sampling stars of given masses from the cluster isochrone based on a Kroupa initial mass function (IMF) (Kroupa 2001) using the imf Python package¹, up to a total cluster mass M. Assuming a single, fixed IMF for all of our clusters is a large but fair assumption for our purpose, as recent results have shown that many clusters still appear to retain the imprint of the IMF they formed with (HR24), particularly for high-mass stars (which represent the majority of observed stars at the distances investigated in this study).

Having created a single-age, single-metallicity stellar population, the next step is to simulate spatial and velocity information. We assume that clusters follow a King (1962) spatial profile with a core radius r_c and a tidal radius r_t , also solving for the value of r_{50} for each King profile following the method in HR23. Next, stars are paired into multiple systems based on the relations in Moe & Di Stefano (2017), with secondaries placed near to their primary star based on their computed separation and a random orbital inclination. 3D stellar velocities are then sampled from a Gaussian distribution (King 1966) with a dispersion based on the cluster's mass (Portegies Zwart et al. 2010, hereafter PZ10, their Eqn. 4). We assume that $\eta = 10$ in this equation, and then linearly scale the dispersion based on the assumed virial ratio of a cluster Q (where Q = 0.5 is perfectly virialised.) Aided by astropy's coordinates module (Astropy Collaboration et al. 2013, 2018, 2022), the cluster and its member stars are placed at a Cartesian Galactocentric position (X, Y, Z), with an overall cluster orbit added to individual stellar motions specified initially in cylindrical Galactocentric coordinates with velocities $(V_{\phi}, V_{\rho}, V_{z})$. We use the current Galactocentric frame defaults in astropy, namely: that the Sun is at X = -8122.0 pc and Y = 0 pc (GRAVITY Collaboration et al. 2018), with a height above the plane Z = 20.8 pc (Bennett & Bovy 2019), and Galactocentric velocity $V_X, V_Y, V_Z = (12.9, 245.6, 7.78)$ km/s (Drimmel & Poggio 2018).

Then, this idealised simulated cluster is turned into a simulated cluster observation. Firstly, observed positions and velocities are converted into Galactic coordinates l and b, distance d, and proper motions μ_{α^*} and μ_{δ} . Next, observed stellar photometric values are computed based on the cluster's distance and selected extinction A_V , utilizing the pre-computed Gaia DR3 photometric relations in Anders et al. (2022). Then, the apparent magnitudes of the member stars are used to select similar, real Gaia stars in a region around the cluster, assigning astrometric and photometric errors to cluster member stars and resampling simulated observed astrometry and photometry from a Gaussian distribution. Binaries are converted into unresolved systems and their photometry added when their separation is below 0.6", which is a basic but fair resolution for Gaia based on comparisons of Gaia data to external binary star surveys (Fabricius et al. 2021). Finally, selection effects in the Gaia dataset and the Gaia dataset subsample of HR23 are accounted for, using the Gaia selection function of Cantat-Gaudin et al. (2023) and the subsample selection function of Castro-Ginard et al. (2023) to restrict the observed cluster to only stars that would have been included in the HR23 cluster survey (namely: those in Gaia DR3 with all five astrometric parameters, G, G_{BP} , and G_{RP} photometry, and those with a Rybizki et al. (2022) v1 quality classification of at least 0.5). This concludes the simulation of a cluster.

https://github.com/keflavich/imf

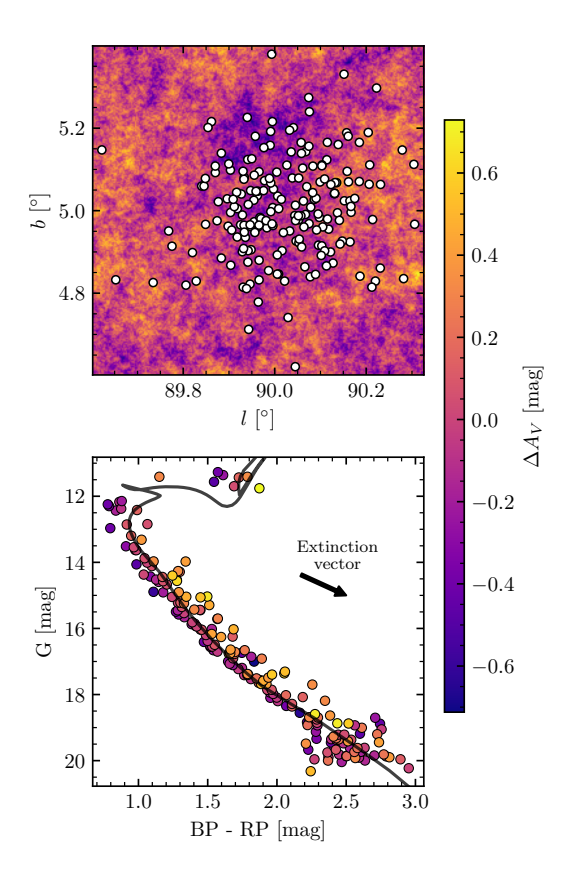


Fig. 1. Example of a simulated cluster with photometry broadened by differential reddening. The cluster has an age of 1 Gyr, a mass of 500 M_{\odot} , an extinction A_V of 1.5 mag, 0.2 mag of differential reddening (measured in colour E(B-V)), and is at a distance of 1 kpc. *Top:* random fractal noise map used to pick a differential reddening for each star. Member stars are shown as white circles, with the coloured background corresponding to changes in extinction A_V . *Bottom:* final simulated CMD for the cluster, including the impact of differential reddening, unresolved binary stars, and *Gaia* photometric errors. Member stars are colour-coded based on their differential reddening with the same colour scheme as the upper panel. The black line shows the isochrone that the cluster's member stars were originally drawn from. The labelled black arrow shows the mean extinction vector for stars in this cluster.

2.2. Additional features for this work

Two notable improvements were made to our cluster simulation code for the purposes of this work. Firstly, we added support for differential reddening to our simulated clusters; secondly, we open sourced our cluster simulation code in the upcoming Python package ocelot², helping to make our results reproducible.

As dust in our Galaxy has a complicated structure (see e.g. Edenhofer et al. 2024), it is common for reddened OCs to have a different amount of extinction in different parts of the cluster, depending on the integrated structure of foreground dust clouds along the line of sight towards each member star. This causes a cluster's CMD to be broadened from the narrow, ideal isochronal line of stellar models. Typically, differential reddening is simulated by applying a random Gaussian-distributed reddening offset to each member star, depending on some amount of differential reddening dispersion (e.g. Hosek et al. 2020), motivated by the generally Gaussian dispersion of reddening values in clusters that have determined per-star extinctions (e.g. Pancino et al.

Table 1. Range in cluster parameters explored in this study.

Parameter	Source	Min.	Max.	Unit
X^a	\mathcal{U}	-23.1	0	kpc
Y^a	\mathcal{U}	-15	15	kpc
Z^a	$0.8 \mathcal{N}(0, 0.25)$	-2.5	2.5	kpc
	$+0.2\mathcal{U}$			-
V_R	$0.8 \mathcal{N}(0,35)$	-150	150	km s ⁻¹
	$+0.2\mathcal{U}$			
$V_{\phi-{ m circ}}$	$0.8 \mathcal{N}(0, 25)$	-150	150	km s ⁻¹
,	$+0.2\mathcal{U}$			
V_Z	$0.8 \mathcal{N}(0, 15)$	-100	100	$km s^{-1}$
	$+0.2\mathcal{U}$			
M	Power laws ^b	40	50000	${ m M}_{\odot}$
$\log t$	\mathcal{U}	6	10	dex
[M/H]	$\mathcal U$	-1	0.5	dex
A_V	dust maps	0	20	mag
$\Delta A_V/A_V$	\mathcal{U}	0	0.5	mag
Q	$\mathcal{N}(0.5, 4)$	0.1	10	_
r_c	\mathcal{U}	0.1	8	pc
r_J	gal. potential	_	_	pc
r_t/r_J	u	0.5	2	_

Notes. \mathcal{U} denotes a uniform distribution between the minimum and maximum value. $\mathcal{N}(a,b)$ denotes a normal distribution truncated between the minimum and maximum value, with mean a and standard deviation b. For some parameters, a weighted combination of both distributions was used. (a) Samples with a total heliocentric distance d>15 kpc or d<0.5 kpc were discarded. (b) Sampled from a broken power law that favoured low-mass clusters and is flat at high masses; that is, one with slopes (in mass order) of -1.013, -2.606, and 0.0, with break points at 813 M_{\odot} and 3364 M_{\odot} .

2024). However, differential reddening is spatially correlated across real clusters, with stars in similar positions having similar levels of reddening. This can lead to complicated changes in the shape of clusters as certain parts of a cluster are reddened out of view (Cantat-Gaudin & Anders 2020, their Fig. C.1), which is not otherwise simulated by non-spatial differential reddening. 3D dust maps also do not have the required resolution to allow for real sub-parsec scale variations in dust to be queried, especially at the high end of distances considered in this study.

Instead, we approximate differential reddening by creating a spatially correlated random noise map for each cluster. We do so with the common signal processing concept of fractal noise (also known as 1/f or 'pink' noise Bak et al. 1987), a type of noise where power density is inversely proportional to frequency. This noise can be easily and quickly generated, and when used to select differential reddening values, the resulting dispersion in perstar differential reddening remains Gaussian – except now spatially correlated. An example of a cluster differential reddening noise map and the resulting cluster CMD is shown in Fig. 1. As a final motivation for this technique, we note that the chaotic and 'cloudy' structure of fractal noise appears similar to the small-scale structure of high-resolution 3D dust maps (Edenhofer et al. 2024).

2.3. Injection and retrievals

With our cluster simulation pipeline in hand, the last step in our method was to perform a collection of injection and retrieval experiments. We followed the clustering method of Paper I, which in turn replicated the clustering method of HR23 as closely as possible. Unlike in Paper I, we chose to inject and retrieve just

https://github.com/emilyhunt/ocelot

one cluster at a time, ensuring that simulated clusters can never overlap within clustering fields, preventing 'self-contamination' of our data – an issue more prevalent at the lower distances considered in this study than in Paper I. For each simulated cluster, the HEALPix level five pixel (in Galactic coordinates) of Gaia DR3 data containing it was loaded, in addition to the neighbouring eight pixels around it – creating a 3×3 dataset of nine level five pixels to analyse with the clustering algorithm used by HR23, HDBSCAN (Campello et al. 2013; McInnes et al. 2017). As in HR23, each dataset's positions and proper motions were then transformed to a bespoke spherical coordinate system centred on its central pixel, minimizing coordinate distortions in position or proper motion data. The positions, proper motions, and parallaxes of each dataset were rescaled into an arbitrary clustering dataset, where where each of the five dimensions of the data has zero median and unit interquartile range to help improve clustering (a step taken by HR23 and various other works, e.g. Castro-Ginard et al. 2018, given that clustering algorithms do not understand units). As in HR23, HDBSCAN was ran with its minimum number of samples parameter fixed to 10, and with the minimum cluster size m_{clSize} at four different values – 10, 20, 40, and 80.

HR23 also included clustering runs at HEALPix level two and in Cartesian coordinates aimed at better detecting the full extent of nearby clusters, as some close clusters (such as the Hyades) are significantly larger than a single HEALPix level five pixel. In this work, we only performed injection and retrievals at HEALPix level five, as HR24 is likely to be 100% complete within the range of which HEALPix level two or Cartesian clustering runs were used (see HR24 Sect. 5.1). Hence, the present work only injects clusters at a minimum distance of 500 pc for reasons of simplicity.

Next, we computed the statistical significance of each cluster compared to their surrounding dataset, using the cluster significance test (CST) from Hunt & Reffert (2021) – a critical step that HR23 used to discard false positives. In their work, only clusters with CST > 3 were retained, meaning that our selection function must establish both the probability that a cluster is detected by HDBSCAN and the probability that it has a CST greater than this threshold. HR23 recommends using a higher CST threshold of five or more when higher-quality cluster samples are required, and so we also record detected cluster CSTs to investigate this further. Cluster CST values were used to select the best cluster detection given our four trialled $m_{\rm clSize}$ values, prioritizing the detection with the highest CST as in HR23.

The distributions that the parameters of injected clusters were sampled from are given in Table 1. Unlike in Paper I, we tried to sample wide ranges in parameters, including exploring if variation in parameters such as [M/H] or Q had an influence on cluster detectability, hence varying a total of thirteen parameters. For parameters such as cluster mass and cluster velocities, we tried to sample parameter ranges wider than the observed OC census, but with more sampling weight applied towards typical cluster values (such as by sampling from a combined Gaussian+Uniform distribution).

Some additional cluster parameters were then computed based on the chosen parameters. For A_V , which is a function of cluster position, we again used the Bayestar19 3D dust map (Green et al. 2019) for most of our sample, in addition to using the relation $E(B-V) = 0.884 \times E(\text{Bayestar19})$ to convert the arbitrary reddening unit used by the Bayestar19 dust map into a

B-V reddening³. To fill in the gaps not observed by the Pan-STARRS 1 survey that Bayestar19 is based on, we also used the Zucker et al. (2025) dust map for an additional ~90° segment of the Galactic plane, plus the Edenhofer et al. (2024) and Lallement et al. (2022) to help fill the pixels outside of the plane not covered by either of the first two maps – although the latter two maps do not go to distances as high as the former two, meaning that the gaps in the Bayestar19 and Zucker map combinations cannot be completely filled with presently available data. For all maps, we assume that the dust curve shape $R_V = 3.1$ – although future studies may wish to incorporate three-dimensional R_V maps, such as that of Zhang & Green (2025), which was released during the preparation of this work.

Our results also rely somewhat on a choice of Galactic potential. In Paper I, we fixed the cluster tidal radius r_t to the cluster Jacobi radius r_J , which gives the expected cluster size based on its mass and the local strength of the Galactic potential. In this work, we introduce a new parameter $[r_t/r_J]$, a multiplier for r_t that allows it to be smaller or larger than r_I , making our results less sensitive to a choice of Galactic potential. Nevertheless, we also opted to use a more recently derived potential for this work – the MilkyWayPotential2022 in gala (Price-Whelan 2017; Price-Whelan et al. 2024, hereafter MW22), which is based on the Eilers et al. (2019) Galactic rotation curve and a range of recent Milky Way mass measurements. We also used the MW22 potential to compute the circular velocity of clusters $V_{\rm circ}$ given their Galactocentric radius R_{GC} , which in turn was added to our sampled $V_{\phi - {
m circ}}$ velocities to compute their actual velocity in the ϕ direction V_{ϕ} .

In total, we ran our full cluster simulation, injection, and retrieval pipeline on 80 590 clusters across around one month of compute time on around 200 CPUs, using code that could run continuously until stopped. 4978 simulated clusters had zero observable stars in Gaia DR3, and were hence recorded as nondetections without running clustering. Of the remaining injected clusters, 870 had membership lists that contained more stars from known clusters in HR23 than from their original simulated cluster. These overlapping cases were discarded, leaving a final dataset of 79,720 clusters. During the fitting of our models, we found that extinction values towards the Galactic centre for the Bayestar 19 dust map (which covers $l > 0^{\circ}$) and the Zucker et al. (2025) dust map (which covers $l < 360^{\circ}$) began to differ significantly at high distances ($d \gtrsim 3$ kpc), which could otherwise bias any selection function model working on either side of $l = 0^{\circ}$ at high distances, which is an unfortunate side-effect of the current lack of a single homogeneous dust map covering the full Galactic plane. Motivated by the fact that HR23 is virtually devoid of OCs in the Galactic centre anyway due to the region's high extinction and crowding, we hence did not use clusters with X > -5 kpc for fitting our final selection function models, leaving a total of 62 143 unbiased simulated cluster retrievals. We publish our cluster injection and retrieval data along with this work, as outlined in Appendix B and available in the online material.

3. Training and validation of selection function models

In this section, we outline the training and validation of our main selection function model. We investigated a number of potential

³ See notes on Bayestar19 reddening unit conversion at http://argonaut.skymaps.info/usage

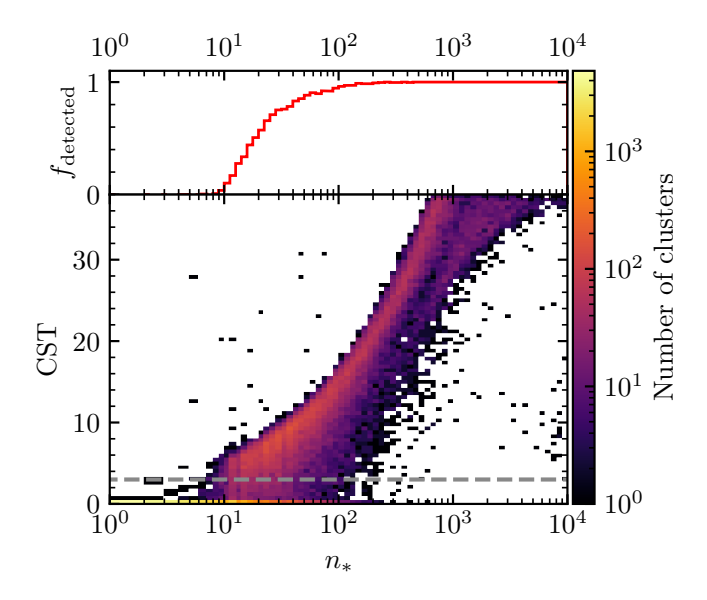


Fig. 2. *Top:* binned mean of f_{detected} against the number of simulated stars injected into *Gaia* data for simulated clusters in this study. See also Fig. A.2 for more examples of the logistic dependence of f_{detected} on n_* . *Bottom:* a 2D histogram of CST against number of injected stars for simulated clusters. The number of clusters at a given point is shown by the logarithmic colour scale. The dashed grey line shows CST = 3, which is the threshold for a cluster to be detected and included in HR23. Only clusters with a CST below 38 are shown; values larger than 38 are calculated as infinity by our Python method due to floating point precision reasons.

models and frameworks, aiming to create a method that could be easily replicated in future works for future cluster catalogues.

In Paper I, we parameterised our cluster selection function based on a number of cluster parameters, including their mass, distance, extinction, and age. For this work, we settled on a somewhat different, 'split' approach: our selection function is instead parameterised on the true number of member stars of a cluster in Gaia data, n_* , which we explore in this section. This provides two advantages: firstly, the number of stars visible in Gaia data for a cluster is more interpretable, particularly when trying to understand the limitations of one cluster detection method over another; secondly, when the number of stars in a cluster is already known (such as for a cluster that appears in one catalogue but not another), then the selection function of one catalogue could be compared easily against another – and without requiring difficult to determine parameters such as a cluster's mass to be calculated.

In this section, we discuss how we created our n_* -based selection function, in addition to choosing additional parameters to add to our selection function to improve its accuracy, given that there is not a perfect correspondence between n_* and how well a cluster is recovered by HR23's pipeline (Fig. 2). When n_* is not known, a cluster can be simulated based on its parameters to derive it (see Sect. 2); we also provide a model to convert cluster parameters to n_* in Sect. 4, for science cases where simulating clusters would be too time-consuming or impractical.

3.1. Map of Gaia data density

As in Paper I, parameters such as a cluster's extinction, age, distance, and orbit proved influential for whether or not a cluster is detected. To potentially reduce the dependence of our model on

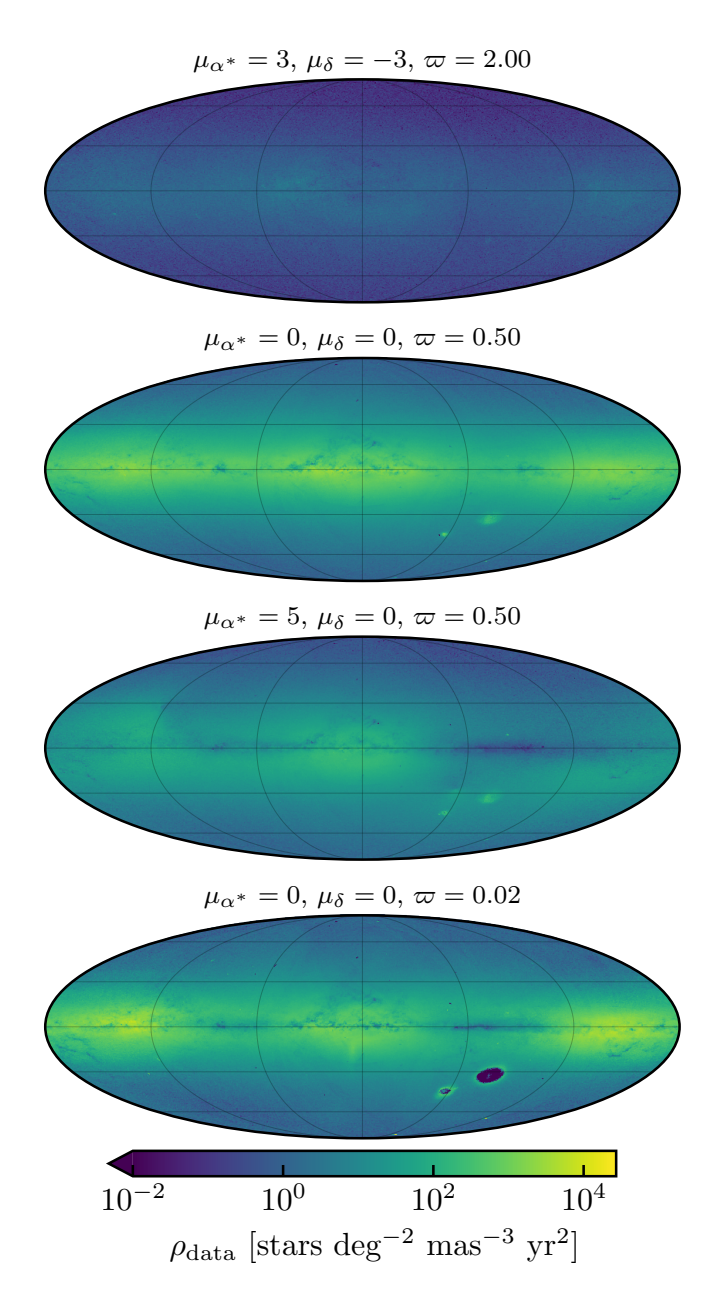


Fig. 3. Four maps of *Gaia* data density at various different proper motion and parallax levels. The proper motion and parallax values of each subplot are indicated in the titles, with proper motions given in mas yr^{-1} and parallax in mas. Maps are plotted in a Mollweide projection in Galactic coordinates, with l increasing to the left, north up, and the Galactic centre in the middle. Vertical and horizontal grid lines show spacings of 60 and 30 degrees in l and b respectively.

difficult to determine cluster parameters, we also experimented with including many other parameters, such as various measures of the density of Gaia data around the cluster ρ_{data} , the median magnitude of cluster member stars, or their median uncertainty in parallax $med(\sigma_{\varpi})$ (which is a proxy for their overall scatter in the astrometric space clusters are detected in).

To determine the density of *Gaia* data in a repeatable, fast way, we measured the five-dimensional astrometric density (i.e. density in position, proper motion, and parallax-space) of the HR23 sample of *Gaia* data in a HEALPix level 7 map. Instead of measuring the density of *Gaia* data at every possible proper motion and parallax, which would result in an extremely large and

cumbersome map totalling tens or hundreds of GB in size, we instead only store the mean and covariance matrix of proper motions at given parallax values for stars in each HEALPix pixel. The density of HR23's sample of Gaia data at an arbitrary position, proper motion, and parallax can then be estimated quickly as the value of a Gaussian probability density function based on these values. We measure the proper motion mean and covariance values in parallax bins of width 0.1 mas from 0 to 2 mas, corresponding to the full distance range in our study. To improve resilience against stars with outlier proper motions, we also sigma clip stars with proper motions more than 6σ away from the mean proper motion in a given range. We linearly interpolate proper motion mean and covariance values between parallax bins to ensure smoothness of our map. This results in a map with 196 608 pixels that each have 21 parallax bins, which can be efficiently queried using the Python package accompanying this work at a rate of around 10⁵ points per second.

Figure 3 shows four example all-sky queries of this density map: one for a nearby parallax, two for a parallax of 0.5 mas, and one for a distant parallax corresponding roughly to the distance of the Magellanic clouds. The maps show clear increase in *Gaia* data density with increasing parallax. Comparing the second and third maps shows one example of how changing proper motion causes asymmetric changes in *Gaia* data density that depend on the fundamental distribution of stellar orbits in the Milky Way, with the proper motion of μ_{α^*} of 5 mas yr⁻¹ of the third map reducing density the most on the right of the Galactic centre.

These maps illuminate an important caveat of our present selection function. Our density method fails in the vicinity of existing 'clusters' (in the dataset sense), shown for instance around the Magellanic clouds (bottom-right of fourth map in Fig. 3). In these cases, the 'cluster' in *Gaia* data (i.e. the Magellanic clouds) is more numerous than field stars, causing it to dominate the derived density distribution. This could only be fixed by having a mixture model of density components in every HEALPix bin, which is beyond the scope of this work; instead, we note that the selection function of whether a cluster that is next to an existing cluster would be reported as a separate object or not in HR23 is too complicated to determine anyway (Paper I), as cluster separation was a mostly manual process in HR23 that is impossible to exactly replicate, and only impacts a small number of objects. The selection function of clusters in close proximity of one another is a known caveat of our work (Sect. 6) that should be addressed in the future, particularly through improved construction of cluster catalogues that could ease determination of their selection function (Sect. D). In any case, none of the clusters in our training sample are close enough to the Magellanic clouds that issues with our density measure in that region impact them.

We queried $\rho_{\rm data}$ for our injected and retrieved clusters with this map. Then, we proceeded to trialling different selection function models.

3.2. Selection of model parameters

To find the other most important parameters governing the cluster selection function along with n_* , we trained XGBoost models (Chen & Guestrin 2016) on cluster parameters and cluster n_* values to investigate which parameters influenced cluster detectability, in addition to making histograms showing cluster detectability as a function of cluster parameters to gain further intuition (Fig. A.1). For all models, we report their accuracy after optimizing their parameters with Optuna (Akiba et al. 2019), ensuring that our reported tests use the optimal XGBoost parameters.

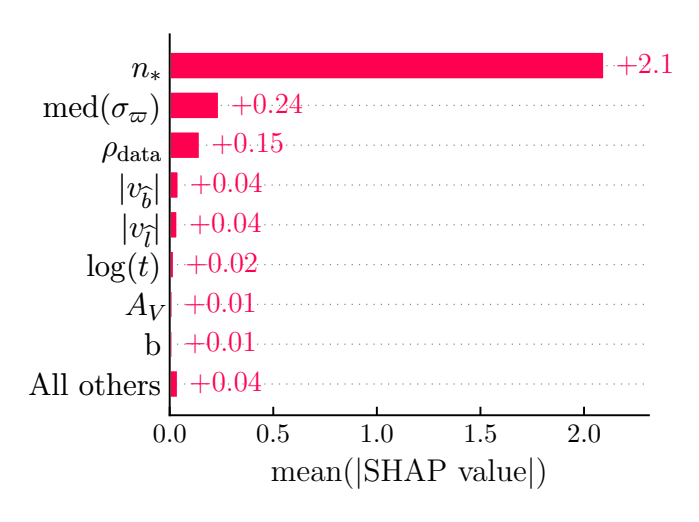


Fig. 4. Mean absolute SHAP values of the XGBoost model used to investigate different selection function parameters in Sect. 3.2.

We augment our data in three ways. Firstly, our sample is divided into training and test datasets comprising 80% and 20% of our simulated clusters respectively. Next, as clusters with zero stars in *Gaia* data are never detected, and clusters with more than 1000 stars appear to always be detected, we trained our models only on clusters with $1 \le n_* \le 1000$, which improved inference speed with negligible loss of accuracy. Finally, we introduced an additional parameter τ , which is a user-defined CST threshold for a cut on the HR23 catalogue, and we chose a random value of τ between one and ten for each cluster to check its detectability at – hence allowing our models to work both for the default CST cut in HR23 ($\tau = 3$), for higher CST cuts for more high-quality samples, and also for lower CST cuts to probe which clusters are only just missing from inclusion in HR23.

We found that just the median parallax uncertainty $med(\sigma_{\varpi})$ and density of Gaia data ρ_{data} alone could explain almost all of the additional variance in cluster detectability, shown in Fig. 4 using Shapely Additive Explanation (SHAP Lundberg & Lee 2017) values for explaining our XGBoost model's output. This is also demonstrated by comparing model binary classification accuracies (Table 2). Our best XGBoost model trained using just n_* had an accuracy of 90.48%. Including all cluster parameters and additional density or uncertainty measures almost halved the error rate of the model, corresponding to an accuracy increased to 94.68%. Yet a model trained just on n_* , med (σ_{ϖ}) , and ρ_{data} saw almost no drop in classification accuracy despite requiring significantly fewer parameters, achieving 94.60% accuracy. Hence, these three parameters (plus whichever τ value the user chooses) appear sufficient to achieve a high model accuracy; we put remaining inaccuracy down to mostly random luck or chance of whether or not our clustering algorithm detects a given cluster.

3.3. MCMC selection function

Noting that our selection function does not appear to require many parameters, and that the relationship between a cluster's detectability and $\log_{10}(n_*)$ appears to be a logistic (Fig. 2, top panel), we fit a simple logistic model to our results to create our final selection function – which has the advantage of significantly improved interpretability over a machine learning approach. Inspired by Cantat-Gaudin et al. (2023), who also fit a logistic model to derive a selection function for *Gaia* DR3, we

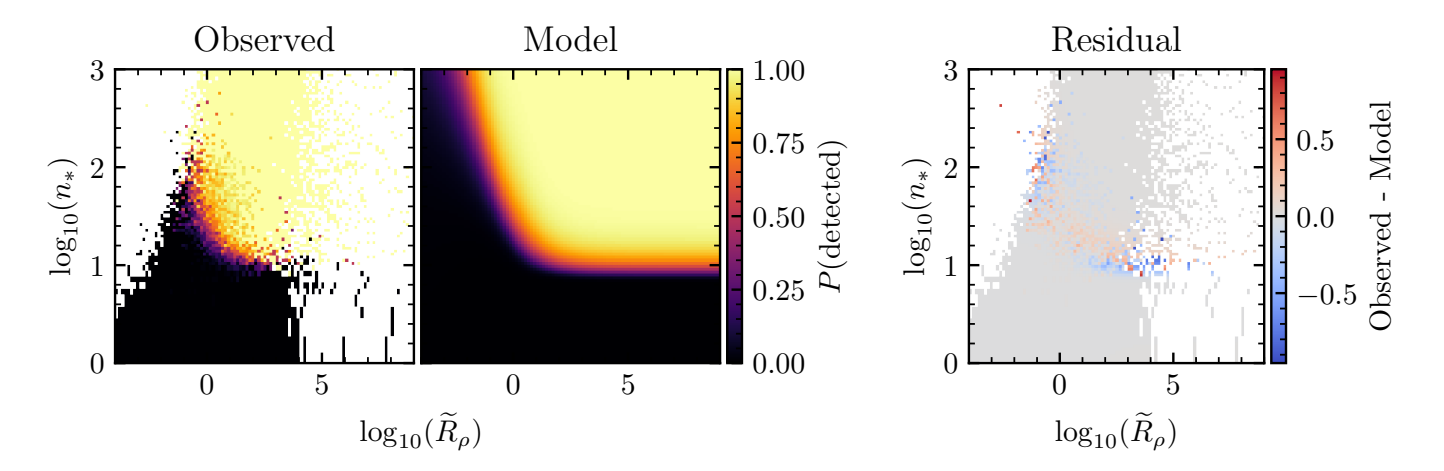


Fig. 5. Comparison between binned P(detected) for various n_* vs. \tilde{R}_ρ values, along with predictions of our selection function model, given $\tau=3$ (the CST threshold for detection of HR23). *Left:* observed distribution of injected and retrieved clusters. *Centre left:* predictions from our model. *Right:* remaining residuals between the model and observed data, where blue corresponds to model overconfidence, red to model underconfidence, and grey to a correct model prediction.

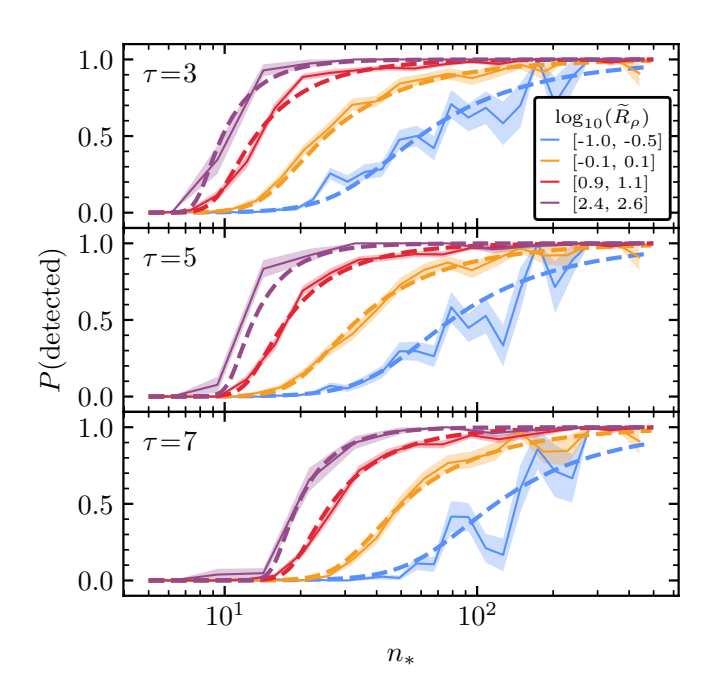


Fig. 6. Comparison between injection and retrieval data (solid line, shaded region shows uncertainty) and our model (dashed line) for various CST thresholds τ and restricted to different density ranges, as indicated in the figure legend. Plots from top to bottom show τ levels of 3, 5, and 7 respectively.

fit a generalized logistic model for the detection probability of a cluster P(detected) of the form

$$P(\text{detected}) = 1 - \left[1 + \exp\left(\frac{\log_{10}(n_*) - a}{\sigma}\right)\right]^{-k},\tag{1}$$

where σ is the width of the logistic, k is a skew parameter that must be greater than zero, and a is an offset to n_* . k=1 corresponds to an unskewed logistic at which a defines the location of the 50% detection probability of a cluster. By default, a and k in this model are highly inter-dependent; to improve how well our model can be fit and interpreted, we instead define a in terms

Table 2. Comparison between XGBoost and MCMC models for predicting cluster detectability from number of stars.

Method	Parameters given	$\mathcal{A}(\%)$	\mathcal{L}
XGBoost	n_*, au	90.48	-2653
XGBoost	$n_*, \tau, \operatorname{med}(\sigma_{\varpi}), \rho_{\text{Gaia}}$	94.60	-1693
XGBoost	All^a	94.68	-1587
MCMC	$n_*, au, ilde{R}_ ho$	94.53	-1672

Notes. ^(a) All cluster parameters and *Gaia* density parameters were given to the model, totalling 19 parameters.

of a more interpretable parameter $n_{*,50}$, which is the number of stars required for a cluster to have a 50% detection probability given k and σ . Rearranging for a when P(detected) = 0.5 and $\log_{10}(n_*) = \log_{10}(n_{*,50})$, this means that a is now given by

$$a = \log_{10}(n_{*,50}) - \sigma \log \left(2^{1/k} - 1\right). \tag{2}$$

Given that $n_{*,50}$, σ , and k could all be arbitrary functions that depend on any of τ , $\operatorname{med}(\sigma_\varpi)$, and $\rho_{\operatorname{data}}$, choosing a correct functional form of each to create an accurate $P(\operatorname{detected})$ equation is non-trivial. Initially, we experimented with using symbolic regression with PySR (Cranmer 2023) to derive functional forms for $n_{*,50}$, σ , and k, given $x = \log_{10}(n_*)$. Although the complexity of the equations PySR derived to achieve our desired accuracy was unsatisfactory, PySR nevertheless helped us gain intuition.

The main insight we gained was to hypothesize that the reason why a cluster is or is not detectable in *Gaia* data can be almost entirely explained by how dense it is compared to the data that surrounds it. Fundamentally, cluster detection in HR23 (or any other cluster detection study with clustering algorithms) depends on how dense a cluster is in *Gaia* data itself. The ratio of the density of a cluster to the density of *Gaia* data at the location of the cluster, $R_{\rho} = \rho_{\rm cluster}/\rho_{\rm data}$, could then be the main other required variable in our selection function.

Defining the density of a cluster ρ_{cluster} is non-trivial, as star clusters have a smooth range of different densities. In position space, their King (1962) density profile smoothly drops from a maximum value to zero; likewise, in astrometric space, clusters have an approximately Gaussian velocity dispersion due to *Gaia*

measurement errors and their internal velocity dispersion. We opt to choose a single, representative value that is straightforward to calculate. Noting that errors on proper motions and parallaxes have a similar order of magnitude in *Gaia* data, and that a cluster's astrometric dispersion is dominated almost entirely by this error, we define an approximate cluster density simply as

$$\rho_{\text{cluster,approx.}} = \frac{n_*}{\text{med}(\sigma_{\varpi})^3},\tag{3}$$

which gives an approximate measure of cluster density in proper motion and parallax space. We also trialled using a measure of cluster size in positions, but this was generally unhelpful – in agreement with our results in Paper I, where we found that the physical size of a cluster has negligible effect on cluster detectability. As ρ_{data} is defined per degree, some correction for area is still necessary to derive physically meaningful R_{ρ} values – so we define our density ratio as 'per-field', dividing by the area of HR23 clustering fields (30.21°) to express R_{ρ} purely in terms of proper motion and parallax density. We hence then define an (approximate) cluster to *Gaia* density ratio as

$$\tilde{R}_{\rho} = \frac{\rho_{\text{cluster,approx.}}}{\rho_{\text{data}}/30.21},\tag{4}$$

and investigate using it as a single variable in the functional form of $n_{*.50}$, σ , and k.

Plotting n_* against \tilde{R}_ρ reveals an intuitive relationship. The left panel of Fig. 5 shows that as \tilde{R}_ρ decreases, n_* needs to increase for a cluster to be detected: a less dense cluster requires more member stars to compensate for its lack of density through quantity of visible members. However, this relationship is nonlinear, and high density values reveal a minimum n_* value below which clusters are only rarely recovered. This minimum value of around ten is likely related to HDBSCAN's minimum cluster size, which had a lowest trialled value of ten in HR23.

We trialled a number of different functional forms for $n_{*,50}$, σ , and k that allowed them to vary as a function of \tilde{R}_{ρ} . We also investigated their dependence on CST threshold τ , finding that this dependence was largely constrained to $n_{*,50}$. Hence, we fit models of the form

$$\log_{10}(n_{*,50}) = g_{n_{*,50}}(\tilde{R}_{\rho}) + u\tau^{\nu} \tag{5}$$

$$\sigma = g_{\sigma}(\tilde{R}_{\rho}) \tag{6}$$

$$k = g_k(\tilde{R}_o),\tag{7}$$

where u and v are constants defining a power-law dependence of $n_{*,50}$ on τ . To allow the three logistic parameters to transition from a single value at high \tilde{R}_{ρ} to a linear relation at low values, we define a smoothing function (similar to a 'softplus' activation function in machine learning) given by:

$$g_x(\tilde{R}_\rho) = \frac{m_x}{|d_x|} \log\left(1 + \exp\left(d_x(\log_{10}(\tilde{R}_\rho) - b_x)\right)\right) + c_x,\tag{8}$$

where x is the variant of the smoothing function, m_x is the gradient of the smoothing function in the increasing part, c_x is a constant defining the minimum or maximum value of the function, b_x is a horizontal offset, and d_x determines how sharp the 'knee' between the flat and increasing parts is, in addition to its orientation. This four-parameter function was found to capture differences between all parameters well. We trialled setting

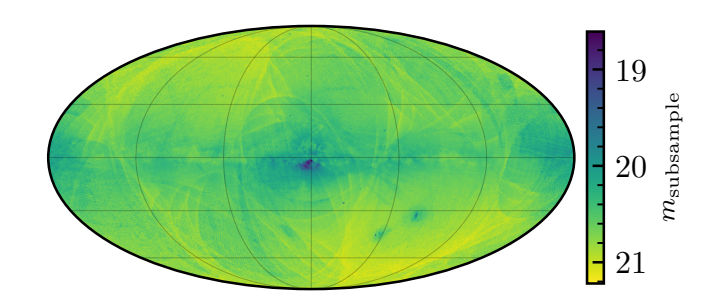


Fig. 7. Map of the median G-band magnitude of stars removed by HR23's Gaia data cuts, $m_{\text{subsample}}$. The map is plotted in the same projection as Fig. 3.

some of the four variables per smoothing function (such as offset b_x or knee sharpness d_x) to be the same for all three logistic parameters, but leaving all four free to vary for all parameters was found to produce a model with the most accuracy.

After setting some relatively uninformative priors on our fourteen model parameters to ensure fitting efficiency and stability (see Table C.1), we fit our selection function model to our data using emcee (Foreman-Mackey et al. 2013), beginning iteration in a small point cloud around the best parameter combination found by Optuna, and using a standard classification log loss \mathcal{L} (see Cantat-Gaudin et al. 2023). We performed 10 000 MCMC steps, discarding the first 1000 as burn-in. Our fitted parameter values and further plots of our model are available in a table and figures in Appendix C, or in the accompanying Python package to this paper that includes our code implementation of this model. Our final model has an overall 94.53% classification accuracy on our training data, which is only marginally lower than the best XGBoost models we trialled, despite using fewer input parameters (Table 2) – validating that our model parametrized only on n_* , \tilde{R}_o , and τ is highly accurate, even compared to machine learning models with far more free parameters.

Comparing the distribution of n_* and \tilde{R}_ρ in Fig. 5 for our injected and retrieved clusters, our model creates a good prediction with minimal residuals, except for around the edges of this distribution that are less well-sampled by our training data. A future iteration of this work could try to sample clusters more uniformly in n_* - \tilde{R}_ρ space to ensure that training data samples this region well. Figure 6 shows that our logistic model closely matches the distribution of our recovered injections and retrievals for a range of different τ CST thresholds.

4. XGBoost n_* predictor

As an alternative to full cluster simulation to transform physical parameters such as mass and age into observed ones n_* and $\operatorname{med}(\sigma_\varpi)$, we also created an XGBoost model to streamline cluster simulation and prediction of n_* and $\operatorname{med}(\sigma_\varpi)$ for certain selection function use cases. While our full cluster simulation suite has been open-sourced in ocelot^4 as a part of this work, it takes approximately one second (not including time to load Gaia data) to simulate a cluster with it – which could quickly become prohibitive for larger works.

We therefore optimized the parameters of an XGBoost model tasked to predict n_* and $\text{med}(\sigma_\varpi)$. For fitting these models, we did not discard clusters at high X as with the selection function – giving us 79 720 clusters, a training sample of 59 790 clusters, and a test sample of 19 930 clusters. We used Optuna to

⁴ https://github.com/emilyhunt/ocelot

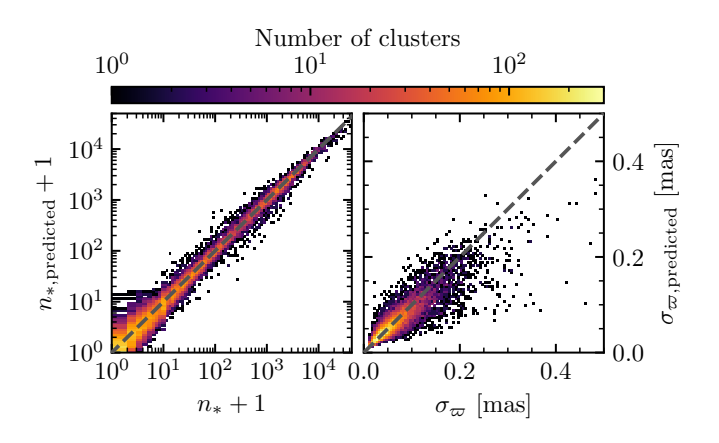


Fig. 8. Accuracy of the XGBoost n_* and σ_{ϖ} predictor in Sect. 4 on its test dataset, with true values on the x axes and predicted ones on the y axes. A perfect prediction falls on the dashed grey line.

optimize model parameters. We set the number of estimators $n_{\tt estimators}$ to be fixed to 100, as larger values dramatically increased training and inference time without significant accuracy improvements. As sampling of the IMF is stochastic, and a given set of cluster parameters does not produce an exact n_* value, we also ensured that this method had quantified uncertainties by creating a bootstrap model ensemble of 250 models trained on independent samples of 66.6% of our training data.

Initially, we trained models that included the cluster parameters M, A_V , ΔA_V , d, $\log t$, and [M/H]. However, as selection effects are significant contributors to incompleteness at the low-mass end, and that these effects are position-dependent, we also incorporated selection effect estimates. Firstly, we included the parameter m_{10} from Cantat-Gaudin et al. (2023), which is the median magnitude of stars that do not appear in Gaia data. In a similar vein, to quantify subsample selection effects for our n_* predictor, we also measured the median magnitude of stars that appear in Gaia but are rejected from HR23's analysis due to their selection of Gaia data, which we denote $m_{\rm subsample}$. Our map of $m_{\rm subsample}$ is shown in Fig. 7.

Finally, we found that changing XGBoost's loss function away from its default produced a less biased model. By default, XGBoost uses mean squared error, which penalises incorrect predictions based on their absolute size – given the large range in n_* in this study (zero to over 50 000), this generally forced the model to prioritize correct predictions at high n_* values. To instead penalize predictions based on the order of magnitude of how incorrect they are at all n_* values, we instead tasked XGBoost with predicting $\log_{10}(n_*+1)$ (which is conceptually the same as using the mean squared logarithmic error, but with the one added to n_* to account for $\log_{10}(0)$ being undefined). This produced a model that was accurate across the whole range of n_* and $\operatorname{med}(\sigma_\varpi)$ (Fig. 8) which we release with this work.

5. An example selection function use: the impact of a cluster's orbit on its detectability

We plan to explore scientific uses of our selection function in future works. As an illustrative example of our selection function's utility, in this section, we demonstrate use of our full model pipeline, and show briefly how even modest increases to cluster orbital speed can dramatically increase cluster detectability.

Figure 9 shows the detectability of a 2.5 Gyr old 200 M_{\odot} cluster with solar metallicity on a circular orbit, having pre-

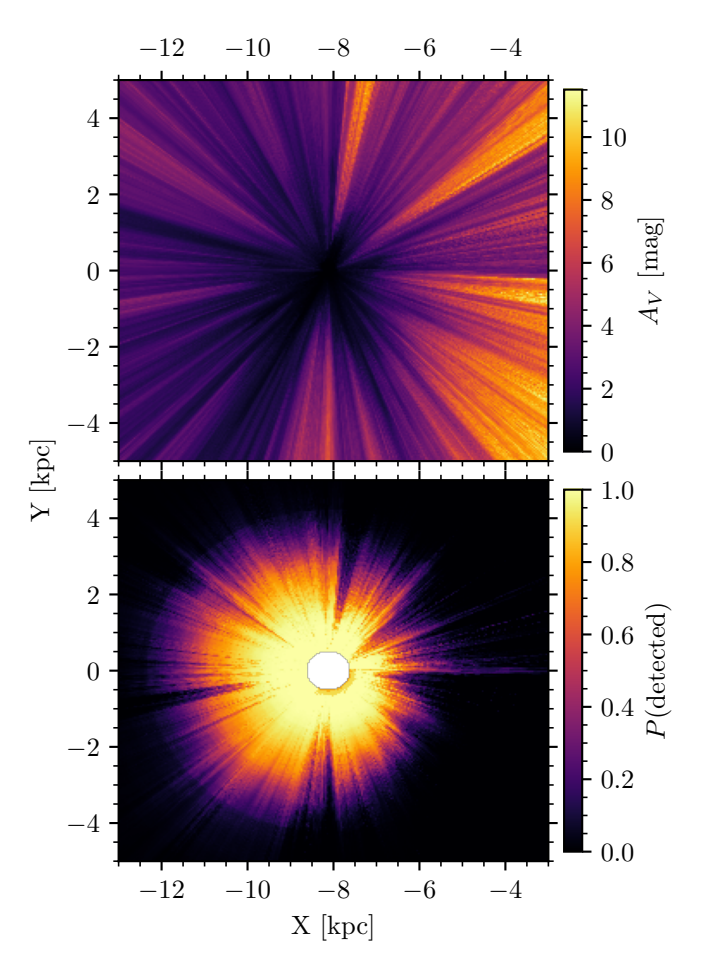


Fig. 9. Example of applying our full selection function pipeline to map cluster detectability. *Top*: adopted dust map viewed top-down in Galactocentric Cartesian coordinates with the Galactic centre to the right, averaged from z values between -100 to 100 pc. *Bottom*: as above, but predicting the detection probability of a 2.5 Gyr old, 200 M $_{\odot}$ cluster with solar metallicity on a circular orbit. n_* and med(σ_{ϖ}) were predicted with our XGBoost predictor and then fed to our MCMC selection function model. The white circle in the middle is a masked region, as distances lower than 500 pc are not considered in this study.

dicted its number of stars and median parallax error with our XGBoost model within a 5 kpc box around the Sun. To construct the figure, we queried our selection function for circular orbits with orbital speeds taken from the MW22 potential, also using the Bayestar19 and Zucker et al. (2025) dust maps to estimate extinction in 3D. The figure clearly shows how a cluster with such parameters is effectively completely undetectable to HR24 within around 4 kpc of the Sun. The 'fingers of god' effect in Fig. 9 is caused by foreground extinction, which causes certain lines of sight to be harder to see clusters along.

We show how detectability of such a cluster can be boosted by non-circular orbits in Fig. 10, which shows the increase to detectability from a 25 km/s boost to the cluster's orbital speed within a few kpc of the Sun, shown for a boost in each of the three Galactocentric cylindrical coordinates. Even for a modest 25 km/s speed boost, which is well within the range of scatter in the observed cluster velocity distribution (Tarricq et al. 2021), cluster detectability is significantly boosted by faster-than-circular cluster orbits. Particularly in the z (vertical) and ϕ (in direction of disk rotation) directions, this boost can cause the example cluster to be almost three times easier to detect.

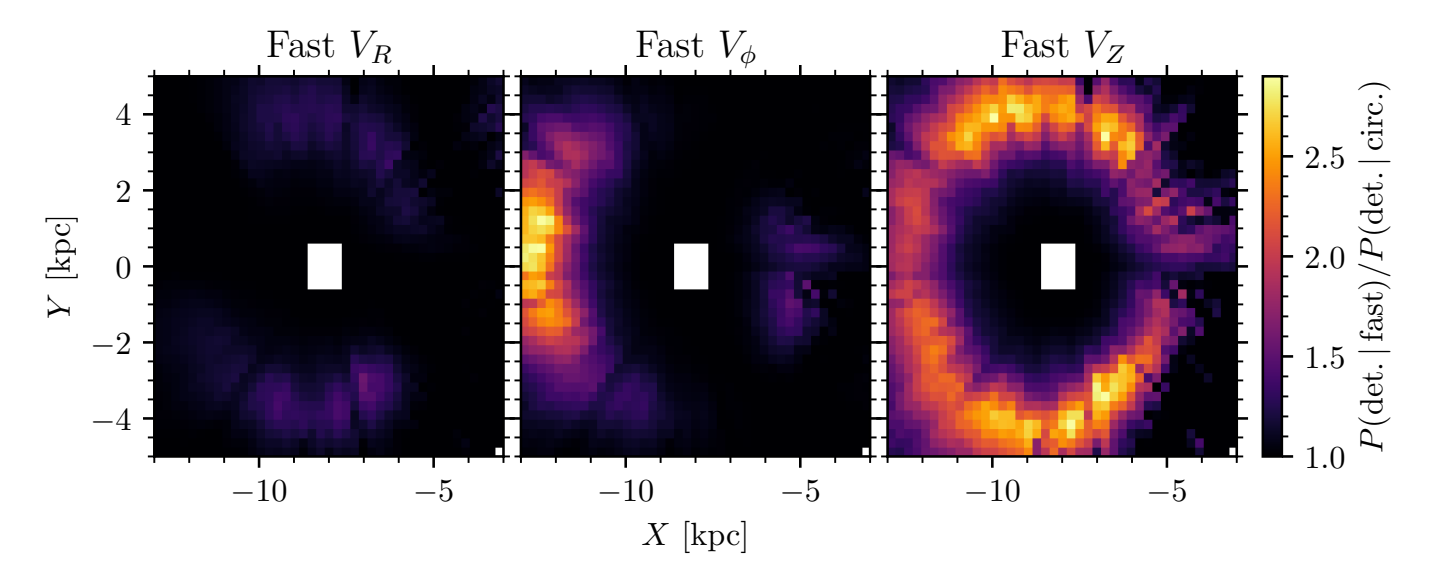


Fig. 10. Impact of cluster detectability from clusters being on non-circular orbits, shown for the same cluster as in Fig. 9 and plotted in the same coordinate system. From left to right, plots show the factor by which cluster detection probability is increased by applying a 25 km/s boost to cluster orbital speed in the radial (*left*), ϕ (*centre*), and Z (*right*) directions, averaged from z = -100 pc to z = 100 pc. The white region in the middle is for distances lower than 500 pc (which are not considered in this study).

The magnitude of this boost is strongly direction and distance-dependent, with a complicated polar detectability pattern imprinted on the ϕ and ρ directions, strongest when all of the cluster's 3D velocity boost goes towards the direction of proper motions measured by Gaia (radial velocities are not used by HR23 for clustering). In addition, the detectability increase of a boost likely also depends on background stellar motions: boosts to the Z and ϕ direction are weakest towards the Galactic centre, probably because the Galactic bulge is both denser and has high scatter in stellar orbits. For clusters that are easier to detect (i.e. younger or more massive ones), this result and shape still holds – the ring of increased detectability is simply shifted to higher distances.

The impact of orbit on cluster detectability across the Galactic disk suggests that recent results using the OC census to trace the velocity distribution of OCs may need to reviewed. The complicated polar pattern of detectability boosts would cause the tails of the overall orbital velocity dispersions of OCs to appear wider than they actually are, as clusters with extreme orbits are more easily detected. Even worse, this polar pattern aligns somewhat with local spiral arms (Poggio et al. 2021; Castro-Ginard et al. 2021; Zucker et al. 2023). Particularly towards the anticentre, a boost to V_{ϕ} can significantly increase cluster detectability; however, these regions also correspond to the location of known spiral structure. Similarly, clusters moving quickly in the ρ direction in the inter-arm region ahead and behind the Sun's orbit will also receive a boost. Any study using the census of OCs to trace the velocity imprint of spiral arms would find that the arms away from and towards the Galactic centre have higher than expected dispersion in V_{ϕ} ; on the other hand, the local arm containing the Sun will appear to have more radial (towards the Galactic centre) dispersion ahead and behind the Sun's orbit. A ring around the Sun will also have higher than expected dispersion in V_Z .

In general, in Galactic dynamics, it is common to assume that velocity distributions are easier to infer than spatial ones, as samples can usually be assumed to not have a detection bias as a function of their velocity (e.g. Tarricq et al. 2021; Alfaro et al. 2025). While this assumption holds for stars, as their probability of inclusion in a dataset is entirely brightness-dependent (Hunt

& Vasiliev 2025), more care must be taken for OCs in the *Gaia* era: proper motions are an essential component of detecting clusters in *Gaia*, but this means that fast-moving clusters are more likely to be detected than slow-moving ones, causing any simple measurement of the dispersion of the cluster census to be biased.

6. Caveats and advice for effective use of our model

Before using our selection function in future work, it is worth recapitulating and explicitly stating some of the caveats of our selection function. Firstly, and most obviously, it is only valid within the cluster parameter ranges that we explored in this work (Table 1); works interested in clusters with parameters outside of this range, or clusters that do not follow a King profile (such as dissolved or unbound clusters), are not guaranteed to receive correct predictions from our selection function.

A second caveat of our work is that we cannot replicate all aspects of the HR23 and HR24 cluster catalogue pipelines. In particular, HR23 ran a large number of different clustering runs in different fields which had to be merged back together. Although this was a well-tested and mostly automated process, it is still possible that some clusters could have been lost in this process, or in other aspects of the HR23 cluster catalogue pipeline. We caution that our selection function is not a definitive answer on whether or not an individual cluster should appear in HR23, and errors could exist in a limited number of cases. We provide some recommendations for future cluster blind searches that would alleviate these issues in Appendix D.

A third caveat of our work is that it only predicts the probability that a real cluster appears in HR23 (i.e. the true positive rate), and not the probability that a false one appears there (i.e. the false positive rate). In principle, the CST cut and CMD classifier from HR23 and object classifications from HR24 can aide with restricting their catalogue to a sample of only high-quality, highly likely to be real objects, and we refer the reader to HR23 and HR24 for discussions of best practices for using these parameters. Our selection function allows for the setting of different CST thresholds τ , and we recommend taking advan-

tage of this for future studies – for instance, by setting $\tau=5$ or $\tau=10$ and cutting HR24 based on that level (in addition to restricting it to only objects classified as open clusters), hence working only with a particularly high-quality sample of their work. If computationally possible, we recommend that works try running their analysis at a few different τ levels, explicitly reporting whether or not using different samples of HR24 causes a qualitative change to their results that could be a result of false positives that emerge at low τ levels.

The final caveat of our work is that many aspects of using our selection function rely on accurate cluster parameters being available, which may often not be the case. In this paper, we have effectively reduced our selection function's dependence on cluster parameters by splitting our selection function into both a function that depends only on basic *Gaia* observables $(n_*, \rho_{\text{data}}, \rho_{\text{data}})$ and $med(\sigma_{\varpi})$), which can be used in cases when these parameters are already known, as well as separate tools for simulating clusters or predicting n_* for when a use case needs to work with more basic cluster parameters. This second use case is much more vulnerable to this caveat. For instance, 3D dust maps must be used to estimate the extinction towards a hypothetical cluster, and so any science case working in this way is only as good as currently available 3D dust maps - all of which have limited distance and angular resolution, and none of which can confidently cover the entire Galactic plane out to more than a few kpc. Similarly, when using cluster parameters in HR24, it is important to appreciate that cluster parameters remain far from perfect, and depend strongly on adopted methodology and cluster membership (Cantat-Gaudin & Casamiquela 2024; Cavallo et al. 2024).

Future studies improving cluster parameters and 3D dust maps further would help to alleviate this final caveat, and such works should continue to be pursued – particularly as the present paper sits on the horizon of many upcoming data releases that will greatly aid in 3D dust mapping and cluster parameter determination. We encourage parameter-determination studies to develop and apply their method to all clusters in HR24, and not just a subset of clusters, as this avoids needing to account for yet another selection function.

With *Gaia* DR4 scheduled to be released in December 2026 at the time of writing⁶, it is likely that new, expanded cluster catalogues will become available soon. We hope to see our work repeated on future data releases and catalogues; in that vein, we also list some recommendations for future selection function studies in Appendix E that will aid in their construction.

7. Conclusions

In this work, we established the first ever global selection function of the OC census, which is valid for the HR24 catalogue. Building on our work in Paper I, we created an accurate cluster simulator and open sourced it in the ocelot Python package. We performed 80 590 cluster injection and retrievals into *Gaia* DR3, varying a wide range of different parameters in order to thoroughly investigate cluster detectability. Next, we created a fast way to look up *Gaia* data density at a given location, proper motion, and parallax, and used it to create a cluster selection function that depends only on a cluster's number of stars, *Gaia* data density, a cluster's median parallax error, and a chosen cluster

significance cut of the HR24 catalogue. In addition to our cluster simulator, we also provide a fast XGBoost model to predict a given cluster's number of stars and median parallax error based on its parameters.

In the spirit of open science, we have open sourced our cluster simulator and selection function for use of the community. Our selection function is available as a Python package⁷. We also release the results of our injection and retrieval experiments, providing a large catalogue of simulated cluster injection and retrievals. These raw data can be used to extend our present work, such as by investigating cluster membership list incompleteness and purity (see example in Appendix F). To aid in use of our work, this paper includes an explicit caveats section aimed to inform users of best practices when using our results.

OCs have been widely catalogued for hundreds of years, but a thorough understanding of exactly how many are contained in a present-day catalogue had so far been elusive. Our work will enable a number of brand new, selection effect-corrected studies to be conducted. We briefly demonstrated one such utility of our selection function in this work, showing that the detectability of OCs is strongly impacted by their proper motion (i.e. speed and direction of Galactic orbit) – showing that previous results that utilized cluster velocities directly will have derived biased properties about the cluster census. Our work will also enable better comparisons between the Milky Way and other galaxies, which is timely given recent strides in the cataloguing of extragalactic clusters, such as through the PHANGS survey (Maschmann et al. 2024). Parameters such as the cluster age and mass function (e.g. Anders et al. 2021; Hunt & Reffert 2024; Almeida et al. 2025) could now be derived as a function of Galactocentric radius, and compared against other galaxies.

Our fundamental objective with this short paper series was to investigate if the selection function of the OC census is computationally possible to derive. With this work, we hope to have resoundingly demonstrated that. We encourage future authors of cluster catalogues to use our methodology, and to continue to derive OC catalogue selection functions for their catalogues based on upcoming surveys and data releases.

Acknowledgements. ELH thanks Hans-Walter Rix for helpful discussions. This work has made use of data from the European Space Agency (ESA) mission Gaia (http://www.cosmos.esa.int/gaia), processed by the Gaia Data Processing and Analysis Consortium (DPAC, http://www.cosmos.esa.int/ web/gaia/dpac/consortium). Funding for the DPAC has been provided by national institutions, in particular the institutions participating in the Gaia Multilateral Agreement. This work was (partially) supported by the Spanish MICIN/AEI/10.13039/501100011033 and by "ERDF A way of making Europe" by the European Union through grant PID2021-122842OB-C21, and the Institute of Cosmos Sciences University of Barcelona (ICCUB, Unidad de Excelencia 'María de Maeztu') through grant CEX2019-000918-M. FA acknowledges the grant RYC2021-031683-I funded by MCIN/AEI/10.13039/501100011033 and by the European Union's NextGenerationEU/PRTR. In addition to those mentioned in the text, this work made use of the following software packages: Jupyter (Perez & Granger 2007; Kluyver et al. 2016), matplotlib (Hunter 2007), numpy (Harris et al. 2020), pandas (Wes McKinney 2010; pandas development team 2025), python (Van Rossum & Drake 2009), scipy (Virtanen et al. 2020), astroquery (Ginsburg et al. 2019; Ginsburg et al. 2025), Cython (Behnel et al. 2011), dustmaps (Green 2018; Green et al. 2024), galpy (Bovy 2015), h5py (Collette 2013), Numba (Lam et al. 2015; Lam et al. 2024), scikit-learn (Pedregosa et al. 2011; Buitinck et al. 2013; scikit-learn developers 2025), seaborn (Waskom 2021), and tqdm (da Costa-Luis et al. 2024). This research has made use of NASA's Astrophysics Data System. Some of the results in this paper have been derived using healpy and the HEALPix package⁸ (Zonca et al. 2019; Górski et al. 2005; Zonca et al. 2024). Software citation information aggregated using The Software Citation Station (Wagg & Broekgaarden 2024; Wagg et al. 2025). This work used the accessible Matplotlib-like colour cycles defined in Petroff (2021).

⁵ We did not establish the selection function of HR23's CMD classifier in this paper; their CMD classifications are an optional catalogue filter that can result in genuine clusters that have broadened CMDs from young age or embedded status being removed (Quintana et al. 2025).

⁶ https://www.cosmos.esa.int/web/gaia/release

⁷ https://github.com/emilyhunt/hr_selection_function

⁸ http://healpix.sourceforge.net

References

- Akiba, T., Sano, S., Yanase, T., Ohta, T., & Koyama, M. 2019, in Proceedings of the 25th ACM SIGKDD International Conference on Knowledge Discovery and Data Mining
- Alfaro, E. J., Sánchez-Gil, M. C., & Elmegreen, B. 2025, Monthly Notices of the Royal Astronomical Society, 537, 3066
- Almeida, D., Moitinho, A., & Moreira, S. 2025, Astronomy and Astrophysics, 693, A305
- Anders, F., Cantat-Gaudin, T., Quadrino-Lodoso, I., et al. 2021, A&A, 645, L2 Anders, F., Khalatyan, A., Queiroz, A. B. A., et al. 2022, Astronomy and Astrophysics, 658, A91
- Astropy Collaboration, Price-Whelan, A. M., Lim, P. L., et al. 2022, The Astrophysical Journal, 935, 167
- Astropy Collaboration, Price-Whelan, A. M., Sipőcz, B. M., et al. 2018, The Astronomical Journal, 156, 123
- Astropy Collaboration, Robitaille, T. P., Tollerud, E. J., et al. 2013, Astronomy and Astrophysics, 558, A33
- Bak, P., Tang, C., & Wiesenfeld, K. 1987, Phys. Rev. Lett., 59, 381 Behnel, S., Bradshaw, R., Citro, C., et al. 2011, Computing in Science Engineering, 13, 31
- Bennett, M. & Bovy, J. 2019, Monthly Notices of the Royal Astronomical Society, 482, 1417
- Bonatto, C., Kerber, L. O., Bica, E., & Santiago, B. X. 2006, A&A, 446, 121 Bovy, J. 2015, ApJS, 216, 29
- Bressan, A., Marigo, P., Girardi, L., et al. 2012, Monthly Notices of the Royal Astronomical Society, 427, 127
- Buitinck, L., Louppe, G., Blondel, M., et al. 2013, in ECML PKDD Workshop: Languages for Data Mining and Machine Learning, 108–122
- Campello, R. J. G. B., Moulavi, D., & Sander, J. 2013, in Advances in Knowledge Discovery and Data Mining, ed. J. Pei, V. S. Tseng, L. Cao, H. Motoda, & G. Xu (Berlin, Heidelberg: Springer Berlin Heidelberg), 160-172
- Cantat-Gaudin, T. & Anders, F. 2020, Astronomy and Astrophysics, 633, A99 Cantat-Gaudin, T. & Casamiquela, L. 2024, New Astronomy Reviews, 99, 101696
- Cantat-Gaudin, T., Fouesneau, M., Rix, H.-W., et al. 2023, Astronomy and Astrophysics, 669, A55
- Castro-Ginard, A., Brown, A. G. A., Kostrzewa-Rutkowska, Z., et al. 2023, Astronomy and Astrophysics, 677, A37
- Castro-Ginard, A., Jordi, C., Luri, X., et al. 2020, Astronomy and Astrophysics, 635, A45
- Castro-Ginard, A., Jordi, C., Luri, X., Cantat-Gaudin, T., & Balaguer-Núñez, L. 2019, Astronomy and Astrophysics, 627, A35
- Castro-Ginard, A., Jordi, C., Luri, X., et al. 2022, Astronomy and Astrophysics, 661, A118
- Castro-Ginard, A., Jordi, C., Luri, X., et al. 2018, Astronomy and Astrophysics, 618, A59
- Castro-Ginard, A., McMillan, P. J., Luri, X., et al. 2021, Astronomy and Astrophysics, 652, A162
- Cavallo, L., Spina, L., Carraro, G., et al. 2024, The Astronomical Journal, 167, 12
- Chen, T. & Guestrin, C. 2016, arXiv e-prints, arXiv:1603.02754
- Collette, A. 2013, Python and HDF5 (O'Reilly)
- Cranmer, M. 2023, arXiv e-prints, arXiv:2305.01582
- da Costa-Luis, C., Larroque, S. K., Altendorf, K., et al. 2024, tqdm: A fast, Extensible Progress Bar for Python and CLI
- Demarque, P. R. & Larson, R. B. 1964, The Astrophysical Journal, 140, 544
- Dias, W. S., Alessi, B. S., Moitinho, A., & Lépine, J. R. D. 2002, Astronomy and Astrophysics, 389, 871
- Drimmel, R. & Poggio, E. 2018, Research Notes of the American Astronomical Society, 2, 210
- Edenhofer, G., Zucker, C., Frank, P., et al. 2024, Astronomy and Astrophysics, 685, A82
- Eilers, A.-C., Hogg, D. W., Rix, H.-W., & Ness, M. K. 2019, The Astrophysical Journal, 871, 120
- Fabricius, C., Luri, X., Arenou, F., et al. 2021, Astronomy and Astrophysics, 649, A5
- Foreman-Mackey, D., Hogg, D. W., Lang, D., & Goodman, J. 2013, Publications of the Astronomical Society of the Pacific, 125, 306
- Gaia Collaboration, Brown, A. G. A., Vallenari, A., et al. 2018, Astronomy and Astrophysics, 616, A1
- Gaia Collaboration, Prusti, T., de Bruijne, J. H. J., et al. 2016, Astronomy and Astrophysics, 595, A1
- Gaia Collaboration, Vallenari, A., Brown, A. G. A., et al. 2023, Astronomy and Astrophysics, 674, A1
- Ginsburg, A., Sipőcz, B. M., Brasseur, C. E., et al. 2019, AJ, 157, 98
- Ginsburg, A., Sipőcz, B., Brasseur, C. E., et al. 2025, astropy/astroquery: v0.4.8 Górski, K. M., Hivon, E., Banday, A. J., et al. 2005, ApJ, 622, 759
- GRAVITY Collaboration, Abuter, R., Amorim, A., et al. 2018, Astronomy and Astrophysics, 615, L15

- Green, G. 2018, The Journal of Open Source Software, 3, 695
- Green, G., Edenhofer, G., Krughoff, S., et al. 2024, gregreen/dustmaps: v1.0.13 Green, G. M., Schlafly, E., Zucker, C., Speagle, J. S., & Finkbeiner, D. 2019, The Astrophysical Journal, 887, 93
- Harris, C. R., Millman, K. J., van der Walt, S. J., et al. 2020, Nature, 585, 357 Hosek, Jr., M. W., Lu, J. R., Lam, C. Y., et al. 2020, The Astronomical Journal, 160, 143
- Hunt, E. L., Cantat-Gaudin, T., Anders, F., et al. 2025, Astronomy and Astrophysics, 699, A273
- Hunt, E. L. & Reffert, S. 2021, Astronomy and Astrophysics, 646, A104
- Hunt, E. L. & Reffert, S. 2023, Astronomy and Astrophysics, 673, A114
- Hunt, E. L. & Reffert, S. 2024, Astronomy and Astrophysics, 686, A42
- Hunt, J. A. S. & Vasiliev, E. 2025, New Astronomy Reviews, 100, 101721
- Hunter, J. D. 2007, Computing in Science & Engineering, 9, 90
- Kharchenko, N. V., Piskunov, A. E., Schilbach, E., Röser, S., & Scholz, R. D. 2013, Astronomy and Astrophysics, 558, A53
- King, I. 1962, The Astronomical Journal, 67, 471
- King, I. R. 1966, The Astronomical Journal, 71, 64
- Kluyver, T., Ragan-Kelley, B., Pérez, F., et al. 2016, in Positioning and Power in Academic Publishing: Players, Agents and Agendas, ed. F. Loizides & B. Schmidt, IOS Press, 87 – 90
- Kroupa, P. 2001, Monthly Notices of the Royal Astronomical Society, 322, 231 Lallement, R., Vergely, J. L., Babusiaux, C., & Cox, N. L. J. 2022, Astronomy and Astrophysics, 661, A147
- Lam, S. K., Pitrou, A., & Seibert, S. 2015, in Proc. Second Workshop on the LLVM Compiler Infrastructure in HPC, 1-6
- Lam, S. K., stuartarchibald, Pitrou, A., et al. 2024, numba/numba: Numba 0.59.1 Lamers, H. J. G. L. M. & Gieles, M. 2006, A&A, 455, L17
- Liu, L. & Pang, X. 2019, The Astrophysical Journal Supplement Series, 245, 32 Lundberg, S. & Lee, S.-I. 2017, arXiv e-prints, arXiv:1705.07874
- Maschmann, D., Lee, J. C., Thilker, D. A., et al. 2024, The Astrophysical Journal Supplement Series, 273, 14
- McInnes, L., Healy, J., & Astels, S. 2017, The Journal of Open Source Software,
- Moe, M. & Di Stefano, R. 2017, The Astrophysical Journal Supplement Series, 230, 15
- Pancino, E., Zocchi, A., Rainer, M., et al. 2024, Astronomy and Astrophysics, 686, A283
- pandas development team, T. 2025, pandas-dev/pandas: Pandas
- Pandey, A. K. & Mahra, H. S. 1986, Ap&SS, 126, 167
- Pedregosa, F., Varoquaux, G., Gramfort, A., et al. 2011, Journal of Machine Learning Research, 12, 2825
- Perez, F. & Granger, B. E. 2007, Computing in Science and Engineering, 9, 21 Petroff, M. A. 2021, arXiv e-prints, arXiv:2107.02270
- Poggio, E., Drimmel, R., Cantat-Gaudin, T., et al. 2021, Astronomy and Astrophysics, 651, A104
- Portegies Zwart, S. F., McMillan, S. L. W., & Gieles, M. 2010, Annual Review of Astronomy and Astrophysics, 48, 431
- Price-Whelan, A., Souchereau, H., Wagg, T., et al. 2024, adrn/gala: v1.9.1
- Price-Whelan, A. M. 2017, The Journal of Open Source Software, 2
- Quintana, A. L., Hunt, E. L., & Parul, H. 2025, Astronomy and Astrophysics, 701, L2
- Rix, H.-W., Hogg, D. W., Boubert, D., et al. 2021, The Astronomical Journal, 162, 142
- Rybizki, J., Green, G. M., Rix, H.-W., et al. 2022, Monthly Notices of the Royal Astronomical Society, 510, 2597
- scikit-learn developers, T. 2025, scikit-learn
- Sim, G., Lee, S. H., Ann, H. B., & Kim, S. 2019, Journal of Korean Astronomical Society, 52, 145
- Tarricq, Y., Soubiran, C., Casamiquela, L., et al. 2021, Astronomy and Astrophysics, 647, A19
- Van Rossum, G. & Drake, F. L. 2009, Python 3 Reference Manual (Scotts Valley, CA: CreateSpace)
- Virtanen, P., Gommers, R., Oliphant, T. E., et al. 2020, Nature Methods, 17, 261 Wagg, T., Broekgaarden, F., & Gültekin, K. 2025, TomWagg/software-citationstation: v1.3
- Wagg, T. & Broekgaarden, F. S. 2024, arXiv e-prints, arXiv:2406.04405
- Waskom, M. L. 2021, Journal of Open Source Software, 6, 3021
- Wes McKinney. 2010, in Proceedings of the 9th Python in Science Conference, ed. Stéfan van der Walt & Jarrod Millman, 56 - 61
- Wielen, R. 1971, A&A, 13, 309
- Zhang, X. & Green, G. M. 2025, Science, 387, 1209
- Zonca, A., Singer, L., crosset, et al. 2024, healpy/healpy: 1.18.0 Zonca, A., Singer, L., Lenz, D., et al. 2019, Journal of Open Source Software, 4, 1298
- Zucker, C., Alves, J., Goodman, A., Meingast, S., & Galli, P. 2023, in Astronomical Society of the Pacific Conference Series, Vol. 534, Protostars and Planets VII, ed. S. Inutsuka, Y. Aikawa, T. Muto, K. Tomida, & M. Tamura, 43
- Zucker, C., Saydjari, A. K., Speagle, J. S., et al. 2025, arXiv e-prints, arXiv:2503.02657

Appendix A: Additional plots of injected clusters and cluster distribution

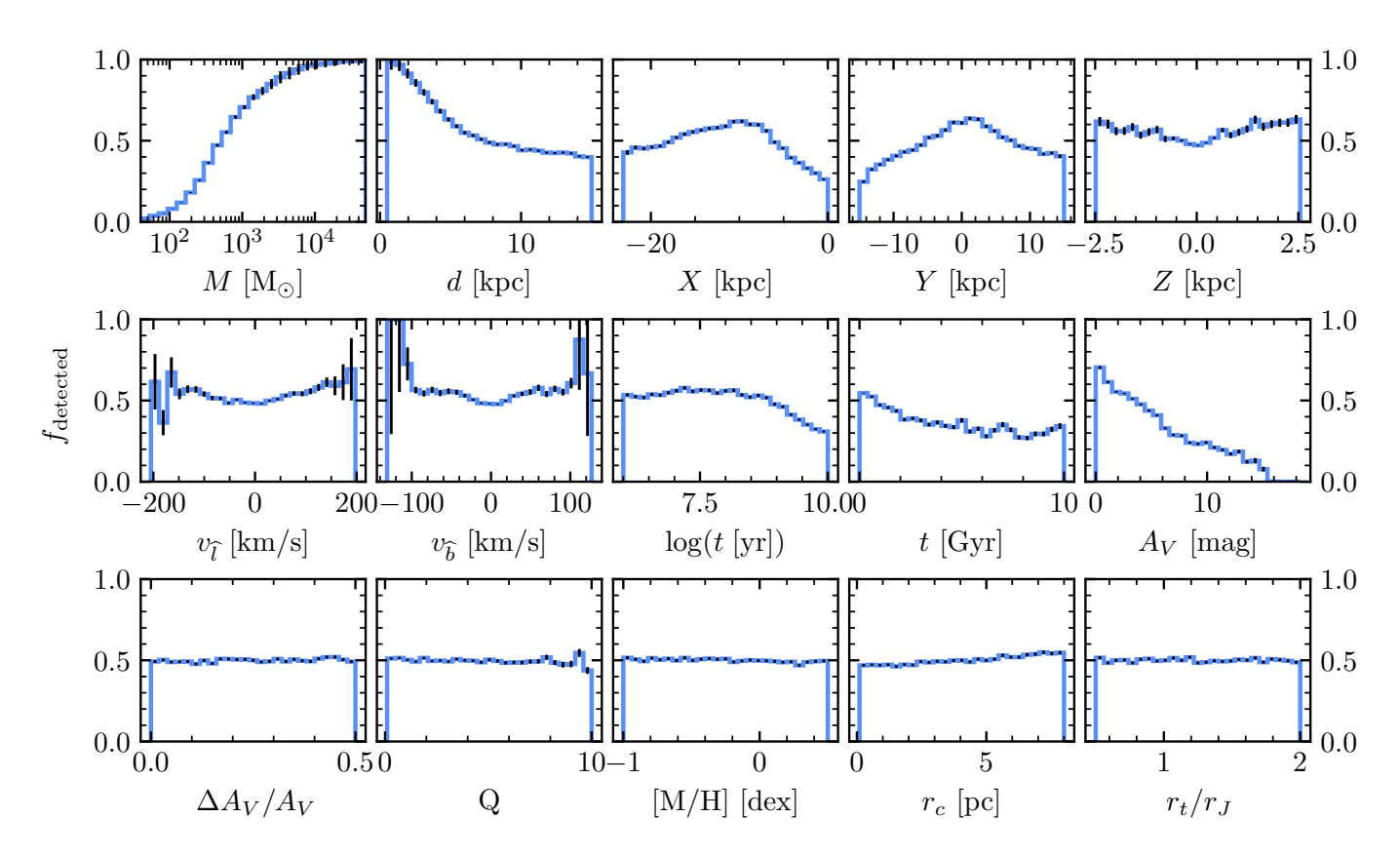


Fig. A.1. Binned fraction of clusters detected at different parameter values for the sample of all 79 720 injected and retrieved clusters. Poisson errors on bins are shown by the black bars.

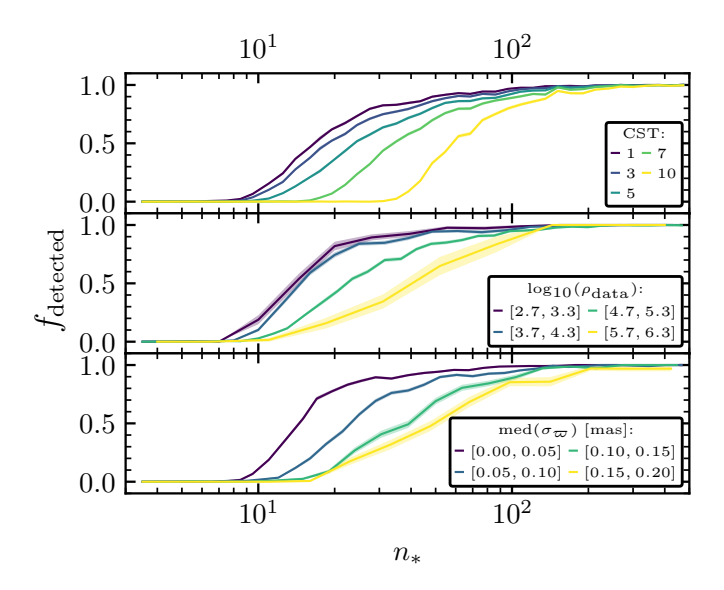


Fig. A.2. Effect of varying cluster sample on the fraction of clusters detected against the number of injected member stars, n_* . Different samples are indicated by the different coloured curves, with the shaded region showing standard error. In the upper panel, CST threshold is varied. In the middle panel, only injected clusters at certain *Gaia* data densities ρ_{data} are shown. In the lower panel, clusters are divided into different samples based on the median parallax error of their simulated member stars.

Appendix B: Published data tables of simulated cluster retrievals

Table B.1. Catalogue of injected and retrieved clusters.

ID	Det. ID	CST	$m_{ m clSize}$	Best?	n_*	$n_{\rm memb.}$	$n_{ m noise}$	<i>l</i> [°]	<i>b</i> [°]	d [kpc]	$M [{ m M}_{\odot}]$	$\log t$	A_V [mag]
							• • •			- 1 -			
1256	_	0.00	_	Y	1	0	0	265	1	10.5	92	6.04	7.44
1257	sZM	9.59	10	N	69	37	4	36	-27	5.0	459	9.84	0.19
1257	AiQ	5.71	10	N	69	12	0	36	-27	5.0	459	9.84	0.19
1257	yQĞ	10.64	20	N	69	83	31	36	-27	5.0	459	9.84	0.19
1257	yQG	10.64	40	N	69	83	31	36	-27	5.0	459	9.84	0.19
1257	yQG	10.64	80	Y	69	83	31	36	-27	5.0	459	9.84	0.19
1258	wnZ	18.11	10	N	187	152	7	76	-27	0.8	176	7.65	0.28
1258	wnZ	18.11	20	N	187	152	7	76	-27	0.8	176	7.65	0.28
1258	wnZ	18.11	40	N	187	152	7	76	-27	0.8	176	7.65	0.28
1258	wnZ	18.11	80	Y	187	152	7	76	-27	0.8	176	7.65	0.28
1259	vVx	2.24	10	N	22	24	12	225	0	10.4	253	8.51	2.08
1259	vVx	2.24	20	Y	22	24	12	225	0	10.4	253	8.51	2.08
1260	_	0.00	_	Y	2	0	0	43	-1	10.1	865	8.00	9.89
1261	rsC	5.80	10	N	38	37	13	204	-2	14.5	935	8.19	2.88
1261	rsC	5.80	20	Y	38	37	13	204	-2	14.5	935	8.19	2.88

Notes. Shown for a subset of fifteen clusters; the full version with all detections and non-detections of all simulated clusters, as well as additional columns, is available online at the CDS. Clusters may be detected at multiple m_{clSize} values by HDBSCAN, with each detection of a cluster being assigned a unique three-character detection ID. As HDBSCAN may report identical clusters even at different m_{clSize} values, these IDs were deduplicated – meaning that one cluster at various m_{clSize} values may share the same detection ID and parameters if they were identical. Clusters not detected at any m_{clSize} value have no detection ID. The 'Best?' column can be used to cut the cluster list to only the best possible detection of each cluster, which was the dataset used to train our model (in addition to later also excluding some clusters based on their X coordinate; see text).

Table B.2. Catalogue of injected and retrieved cluster members.

Simulated cluster ID	Star ID	Detection IDs	DR3 Source ID	G [mag]	$G_{BP}-G_{RP}$ [mag]
			• • •		
_	_	yQG	6904800569939278720	15.24	0.54
_	_	yQG	6904799126830387712	15.38	1.17
1257	1887	sZM,yQG	_	16.40	0.76
1257	1897	sZM,yQG	_	16.76	0.79
1257	1856	sZM,yQG	_	17.26	0.80
1257	2026	sZM,yQG	_	17.31	0.75
_	_	yQG	6904804379573622016	17.69	1.34
1257	1881	sZM,yQG	_	17.83	0.90
_	_	yQG	6904748274417447168	18.31	0.69
1257	1910	sZM,yQG	_	18.37	0.85
_	_	yQG	6904820356852119936	18.49	0.82
1257	2017	AiQ,yQG	_	18.50	0.90
1257	1972	sZM,yQG	_	18.52	0.88
1257	1846	sZM,yQG	_	19.37	1.01
1257	1920	-	_	20.22	1.44
			• • •		

Notes. Shown for just fifteen assigned member stars for simulated cluster 1257 detections; the full version with all stars and all columns is available online at the CDS. To construct a membership list for a given detection, each star should be queried for if it contains the corresponding three-character detection ID. This system is used as a single star may appear in multiple different HDBSCAN detections – including real *Gaia* 'noise' stars. Alternatively, a simulated cluster can be reconstructed by querying based on cluster ID, which will reproduce the original injected cluster membership.

Appendix C: Model fitting results

Table C.1. Fitted model parameters.

Param.	Value	Prior min	Prior max
m_n	$0.771^{+0.006}_{-0.011}$	0.0	10.0
b_n	$2.022^{+0.016}_{-0.018}$	2.0	3.0
c_n	$0.847^{+0.003}_{-0.005}$	0.0	5.0
d_n	$-1.391_{-0.026}^{+0.012}$	-10.0	0.0
m_s	$0.119^{+0.008}_{-0.012}$	-10.0	10.0
b_s	$1.503^{+0.001}_{-0.002}$	1.5	4.5
c_s	$0.012^{+0.001}_{-0.001}$	0.0	10.0
d_s	$-1.700_{-0.358}^{+0.111}$	-10.0	10.0
m_k	$0.014^{+0.008}_{-0.020}$	-10.0	10.0
b_k	$1.554^{+0.038}_{-0.036}$	1.5	4.5
c_k	$0.110^{+0.004}_{-0.013}$	0.0	10.0
d_k	$-9.913_{-0.057}^{+0.054}$	-10.0	10.0
и	$0.006^{+0.000}_{-0.001}$	0.0	1.0
<u>v</u>	$1.678^{+0.009}_{-0.014}$	0.5	4.0

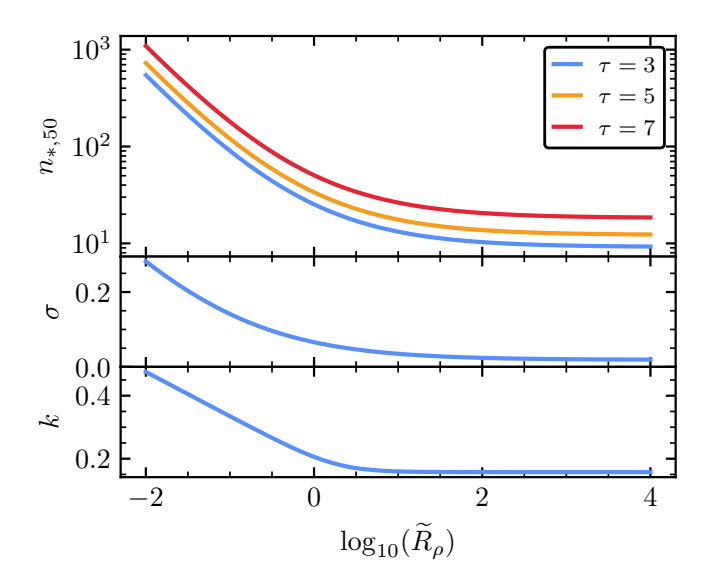


Fig. C.1. Dependence of model parameters $n_{*,50}$, σ , and k on density of a cluster R_{ρ} . For $n_{*,50}$, which also depends on CST threshold τ , three curves are shown: one each for τ of 3, 5, and 7.

Table C.1 presents the results of our model fitting procedure. These parameters are used to derive $n_{*,50}$, σ , and k for our logistic model, which varies with respect to \tilde{R}_{ρ} . This dependence is illustrated in Fig. C.1, showing that the model opts for a steep, skewed logistic function at high \tilde{R}_{ρ} , reducing this to a less certain and symmetric logistic at low \tilde{R}_{ρ} . Since the median number of stars that a cluster needs to be detected in HR23 is a parameter of our model (n_{*50}) , this can also be read directly from Fig. C.1. Indeed, at $\tau=3$, $n_{*,50}$ is around ten, corresponding to the minimum HDBSCAN cluster size used in HR23. $n_{*,50}$ begins to rise when cluster density is about one to two orders of magnitude higher than the density of local *Gaia* data. $n_{*,50}$ rises sharply at low \tilde{R}_{ρ} , with our model predicting that clusters that are 10% as dense as *Gaia* data require at least 100 stars to have a 50% detection chance in HR23 – a full order of magnitude higher than HR23's minimum cluster size.

Appendix D: Advice for future all-sky cluster blind searches

In this section, we discuss some aspects of how HR23 and HR24 were constructed, and how they could be improved in the future to enable easier construction of cluster catalogue selection functions. These improvements could be incorporated into any future blind cluster survey, and not just those following HR23's exact methodology.

Our first difficulty arose with HR23's multiple distance bins. Clustering in HR23 was performed mostly at HEALPix level 5, with fields of nine pixels of around 30 deg² in size. However, capturing the full extent of clusters closer than around 500-750 pc required a separate run with HEALPix level 2 fields containing only stars with $\varpi < 1$ mas, and capturing the full extent of clusters within around 150 pc (which are highly dispersed on-sky) required a Cartesian coordinates run on all stars within 250 pc. These three distance ranges and the 12288 separate pixels at HEALPix level 5 makes reproducing the exact method of HR23 convoluted, due to the large amount of run merging that was necessary in HR23 - our present work hence only establishes HR23's selection function for d > 500 pc and neglects considering the selection function of run merging (Sect. 6). Use of different field sizes to detect clusters of different sizes is also not unique to HR23, having also been a feature of the cluster searches of Castro-Ginard et al. (2018, 2019, 2020, 2022).

Originally, HR23 adopted HEALPix level 5-sized fields to save on computational time, as HDBSCAN's runtime scaling is on order $O(n \log n)$ (in the best cases). This resulted in a total runtime of 8 days to construct HR23 on a modest computational node. Given the widespread use of HR23, expending more computational time to save on later hassle is probably justified. One potential easier strategy for *Gaia* DR4 and beyond would be to have the main runs in a much larger HEALPix size – such as level 2 or 3, resulting in 192 or 768 fields respectively. This would most likely still need to be aided with an additional Cartesian coordinates run to capture nearby clusters such as the Hyades without spherical distortions, but would dramatically reduce the number and complexity of merges required to create a cluster catalogue, trading computational time for ease of processing.

Our next difficulty was with HR23's sample of *Gaia* data. Using a subsample of *Gaia* data is a common, recommended approach that can ensure that unreliable sources are removed before analysis (Gaia Collaboration et al. 2023). Nevertheless, the multitude of cuts applied in HR23 – including the difficult to model machine-learning cut of Rybizki et al. (2022) – make simulating clusters somewhat more complicated. In the future, adopting as few *Gaia* data cuts as possible would likely help. If future *Gaia* data releases see major improvements in the number of stars with erroneous astrometry (particularly at the faint end), then this is likely to be highly feasible.

However, in general, we have found between this work and Paper I that establishing the selection function of a blind cluster search is eminently feasible. Our final recommendation is that cluster surveys do exactly that, using the methodology that we have developed and open-sourced in this work. The cluster census of *Gaia* DR4, *Gaia* DR5, and beyond should also come with an accompanying selection function that is published as soon as possible after publishing the catalogue, allowing for advanced, selection effect-corrected studies of the cluster distribution to be conducted. In the next section, we argue that this is even easier to conduct than we first anticipated.

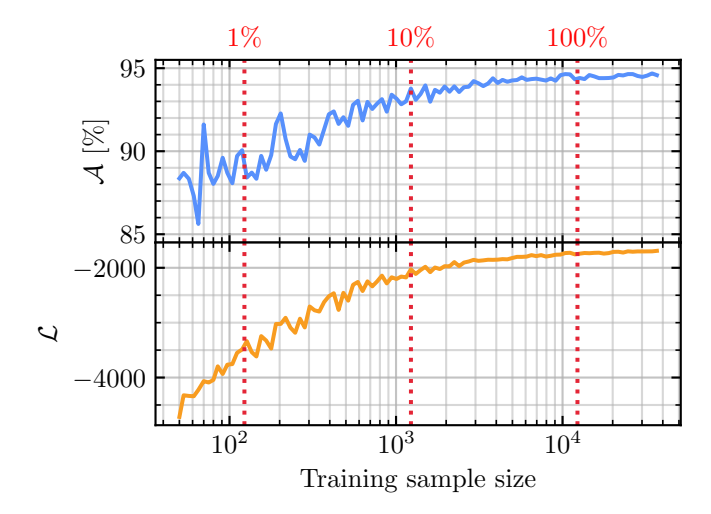


Fig. E.1. Effect of training data sample size on the test data accuracy (upper plot) and test data log loss (bottom plot) of an XGBoost model trained to predict cluster detectability from n_* , τ , med(σ_{ϖ}), and ρ_{data} , as in Sect. 3.2. Red dashed lines, with corresponding labels at the top of the plot, show the size of the training sample as a fraction of the total number of clusters in HR23.

Appendix E: Advice for future cluster selection function studies

Our initial setup for this study and Paper I was based mostly on (educated) guesses. Now, with the benefit of hindsight, we can analyse how effective certain choices were, and identify where future selection studies could be more efficient.

The main insight we can provide is that much less computational time is necessary than we originally thought. Paper I was based on 48 688 clustering runs (of four clusters each) to cover the Galactic anticentre alone, which we found was more than necessary for such a small region. This work was based upon 80 590 clustering runs (of one cluster each) to cover the entire Galaxy – which may still have been more than necessary.

Figure E.1 shows the accuracy of an XGBoost selection function predictor (as in Sect. 3.2) trained on training samples of between 50 to 40 000 clusters, applied to the same test dataset as before. Red dashed lines show the training sample size as a fraction of the original amount of computational work required to do HR23's clustering runs. Even performing around 100 clustering runs can produce a model with almost 90% accuracy. More than 1 000 clusters appears to have diminishing returns, with more than around 10 000 clusters having negligible accuracy improvements. This suggests that a cluster selection function of a full-sky survey with an accuracy on par with this work could be produced by only using about the same amount of computational resources as the original survey, or even less if a few % in accuracy is an acceptable loss. While it may still be necessary to have a larger training sample for an n_* predictor as in Sect. 4 due to its much higher number of input parameters, the comparatively smaller number of input parameters of our selection function (owing to the efficiency of $\rho_{\rm data}$ and ${\rm med}(\sigma_{\varpi})$ in predicting detectability) means that only a surprisingly small training data set is necessary.

This could potentially be improved even further with more efficient training dataset creation. Most clusters simulated in this work are roughly in the middle of the n_* - \tilde{R}_ρ plane in Fig. 5. More efficient training data generation could sample clusters uniformly in these two parameters (instead of uniformly in pa-

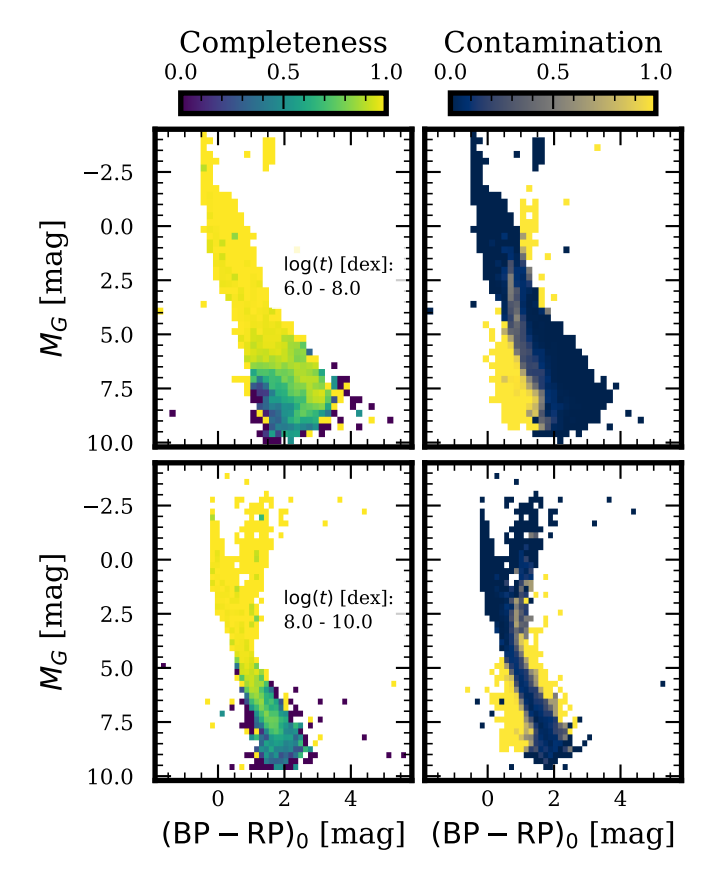


Fig. F.1. Completeness (*left*) and contamination (right) fractions for the derived membership lists of simulated clusters shown in dereddened colour-absolute magnitude diagrams for clusters in log(t) bins of 6.0 - 8.0 dex (top) and 8.0 - 10.0 dex (bottom), respectively.

rameters such as cluster mass or age), creating a smaller training dataset that more efficiently covers relevant \tilde{R}_{ρ} and n_* values required by a selection function. One such setup might simulate a large batch of clusters using the same cluster parameter distributions as in Table 1, also giving a large sample of simulated clusters for study; however, only a small subsample of these (which would then form a uniform n_* - \tilde{R}_{ρ} distribution) would be put forward for clustering runs.

Appendix F: Completeness and contamination of cluster memberships

While the present work aims to investigate the selection function of clusters themselves, studying the completeness and purity of cluster membership lists is equally important for a number of potential applications, such as accurately estimating cluster parameters, cluster binary fractions, and total cluster masses. Moreover, very high contamination rates can lead to some clusters being discarded by the CMD classifiers adopted by HR23 and Castro-Ginard et al. (2019), affecting the completeness of high-quality cluster samples that rely upon them.

In Fig. F.1, we show the membership-level completeness and contamination fractions for a sample of simulated clusters on a colour-absolute magnitude diagram, showing an example of how our additional published data can be used to investigate cluster membership quality. The top and bottom panels correspond to relatively young $(\log(t) \in [6.0, 8.0] \text{ dex})$ and old $(\log(t) \in [8.0, 10.0] \text{ dex})$ ranges in cluster age, respectively,

with other parameters fixed for visualization purposes. As expected, in both young and old simulated clusters, the recovered upper main sequence is fairly complete, with fainter stars increasingly affected by incompleteness due to larger uncertainties in their observed astrometry. This is consistent with the findings of HR24 (see their Fig. 2), who employed a simpler method to compute the probability of inclusion of a true member in the derived membership lists of a given cluster. On the other hand, contamination by field stars affects a broader range of *G* magnitudes, potentially biasing the estimation of cluster parameters and the detection of main sequence—main sequence and white dwarf—main sequence unresolved binaries.

Continued efforts to enhance the purity and completeness of membership lists will be essential to mitigate these effects. We hope that the simulated and recovered cluster membership lists released with this work will serve as a useful benchmark for such future improvements, or as a tool for a future work to derive direct calibration factors for HR24's membership lists.